Advanced NEMS Laboratory

Master Thesis

Aluminum Scandium Nitride as Piezoelectric Material for SAW/BAW Hybrid Resonators with Large Figure of Merit

Professor:
Guillermo Villanueva

Autor:
Guilain Lang

Doctoral assistants :
Soumya Yandrapalli
Marco Liffredo
Damien Maillard

January 14, 2021

EPFL

Abstract

Nowadays, no less than 21 sensors are used to monitor the health conditions of aircraft engines. However, the actual state of technology do not allow the measurements on moving parts in harsh environment (i.e. rotor shaft and blades). Thanks to its straightforward remote capabilities and the exceptional properties of Aluminum Scandium Nitride (AlScN), acoustic resonators based on AlScN thin films are considered the best choice for such application.

Performances of SAW/BAW hybrid resonators based on AlN, AlSc(0.17)N and AlSc(0.40)N were investigated by finite element method in COMSOL Multiphysics.
After noticing the excitation of SAW in AlN/AlScN resonator involves only d_{33}, a series of experiments has been conducted to determine the relation between the design and performances of hybrid resonators. In contradiction with the predictions of previous works, the ratio thickness-over-pitch which maximize k_t^2 seems to be coupled to the etching depth.
Achieving simultaneously a high quality factor ($Q \approx 2000$ $[-]$) and a high electromechanical coupling factor ($k_t^2 = 23.48$ $[\%]$), SAW/BAW hybrid resonators based on AlSc(0.40)N thin film reaches the highest Figure of Merit ever recorded for an AlN/AlScN based acoustic resonators: $k_t^2 \cdot Q = 494$ $[-]$.

Keywords: AlN, AlScN, SAW, BAW, hybrid resonators, parametric study, harsh environment sensing, piezoelectricity, finite element modeling, COMSOL Multiphysics.

Acknowledgments

Foremost, I would like to express my deepest appreciation to my project advisors: my professor, Guillermo Villanueva and my doctoral assistant, Soumya Yandrapalli. Your enthusiasm, knowledge and foolproof motivation in pair with your day to day guidance allowed me to conduct this project almost seamlessly from its acceptance to its conclusion.

Beside my advisors, I would like to thanks all the members of the Advanced NEMS Laboratory for broadening my vision on research, for their insights and for the too few meals we shared together. In particular, I would like to mention the assistance of Marco Liffredo and Damien Maillard without whom my HR Si wafer would still be waiting for Lift-off.

Finally but not least, I would like to express my gratitude to Eva Marlinge, my parents, my sister, my friends from The Countdown Company & the EPFL Rocket Team and my flatmates. I cannot be grateful enough for your daily support, your flawless understanding and all your challenges. I know it can be tough to live and deal with me sometimes. I wouldn't have gone that far if it wasn't thanks to you !

Contents

List of Figures

List of Tables

Definitions and Abbreviations

AlN	Aluminium Nitride
AlSc(0.17)N	Aluminium Nitride doped with 17% Scandium
AlSc(0.40)N	Aluminium Nitride doped with 40% Scandium
AWSN	Airborne Wireless Sensors Network
ANEMS Lab	Advanced MicroElectroMechanical Systems Laboratory (EPFL)
BAW	Bulk Acoustic Wave
CLMR	Cross-Sectional-Lamé-Mode Resonator
CMi	Center of MicroNanotechnology (EPFL)
EPFL	Ecole Polytechnique Fédérale de Lausanne (Swiss Federal Institute of Technology in Lausanne)
FBAR	Film Bulk Acoustic Resonator

FD	Finite Device
FEM	Finite Element Method
FoM	Figure of Merit
FWHM	Full Width Half Maximum
GUI	Graphical User Interface
IDT	Interdigital Transducer
MEMS	MicroElectroMechanical System(s)
PML	Perfectly Matched Layer
Pt	Platinium
SAW	Surface Acoustic Wave
SMR	Solidly Mounted Resonators
SCD	Single Crystal Diamond
Si	Silicon
SiC	Silicon Carbide
TCF	Temperature Coefficient of Frequency
UC	Unity Cell

Chapter 1

Introduction

1.1 Purpose of the Work

Today's, no less than 21 sensors are used to monitor the health conditions of an aircraft engine [2]. However, the actual state of technology do not allow - or at the cost of high integration/-operational complexity - measurements on moving parts (i.e. rotor shaft and blades) in such harsh environment that is gas turbines.
Driven by this demand of the aerospace industry, the Advanced NanoElectroMechanical Systems Laboratory (ANEMS) starts in 2019 a program to develop a novel generation of temperature sensors. Thanks to its heritage on MicroElectroMechanical Systems (MEMS) and its ongoing research on piezoelectric thin films, the ANEMS Lab proposed a robust solution using a Aluminium Scandium Nitride (AlScN) based Surface Acoustic Wave (SAW) resonator.
This Master thesis lays the ground work for the development and optimization of such resonators with high Figure of Merit (FoM).

1.2 Aims and Objectives

Resonators are not restricted to sensing but have a wide variety of other applications such as filters for telecommunication. Therefore, our main aims is to find a novel/optimized SAW resonator based on an Aluminium Nitride (AlN)/AlScN piezoelectric layer which maximize its Figure of Merit (FoM).
The initial title of this master thesis was *Temperature sensor for harsh environments*. Thus, we also aim to develop an optimized SAW resonator to sense the temperature of moving parts in the harsh environment of gas turbines ($T > 800$ [°C]).

No pre-defined objectives have been set, however from the aims cited before and the weekly goals, we can defined the following hierarchy of objectives:

Primary Objectives:

- **Objective A01:** Lay the background to develop a temperature sensor for harsh environment sensing based on AlN/AlScN piezoelectric thin films.
- **Objective A02:** Define a geometry and optimize its parameters to achieve a high FoM.
- **Objective A03:** Determine the effect of these parameters on the resonator's performances.
- **Objective A04:** Define a process flow for the proposed geometry.

Secondary Objectives:

- **Objective B01:** Design a resonator based on a AlSc(0.4)N with a resonance frequency close to 2.45 $[GHz]$.
- **Objective B02:** Manufacture a test device to validate the simulation.
- **Objective B03:** Demonstrate the temperature sensing capability of the designed device.

Tertiary Objectives:

- **Objective C01:** Modelize the relation between the device geometry and its performances/resonance frequency.
- **Objective C02:** Design devices for both standing wave and delay line operations.
- **Objective C02:** Measure the TCF of manufactured devices.

1.3 Structure of the work

This work starts with a review of the literature. In the chapter 2, we present the actual state of the art of AlN/AlScN resonators and some important concepts of resonators in particular on SAW.
Instead of using a finite device (FD) from the beginning, we make a 2D infinite approximation which allow us to compute a lot of designs in a minimum time. The chapter 3 is thus composed of three parts: firstly, we describe the unity cell (UC) simulation setup, then we present preliminary studies used to determine the best geometry. Thirdly, we report a parametric study aiming to determine the parameters' effect onto the performance and to optimize them.
We complexify the simulation in chapter 4 by considering a 2D finite device. It allows us to study the confinement of the wave and evaluate the performances of optimized devices.
Finally, we present some manufacturing considerations in chapter 5 with a process flow, a mask layout and the manufacturing test run review.

Chapter 2

Review of Literature and Definition

2.1 Piezoelectricity and Acoustic Waves

2.1.1 Fundamentals of Acoustic Waves

This section is based on the chapter *2.1.1 - Acoustic Waves* of Campanella's book [3].
In the context of resonators, an acoustic wave is a vibrational perturbation which propagates through time and space in a solid. Through its oscillation, such wave carries mechanical energy which can be either transferred to another location (see two-ports configuration in section 2.2.2) or converted to electrical energy through the piezoelectric effect (see section 2.1.2).

Longitudinal-mode and Transverse-mode Waves

We differentiate the propagation of an acoustic wave from its oscillation. We can imagine one vector which point the direction of the energy transport, this is the propagation direction. A second vector represents the axis along which the particles are vibrating, this is the direction of its oscillation.
With these vectors in mind, we can define a compressive mode when they are co-linear and a shear mode when they are orthogonal. These two fundamental modes are named respectively longitudinal and transverse modes. They are represented in figures 2.1 and 2.2.
NOTE: In general, acoustic waves are neither purely longitudinal nor transverse but a combination of these fundamental modes.

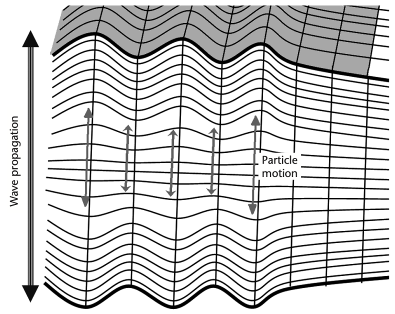

Figure 2.1: Longitudinal-mode waves: the bulk particles oscillate or vibrate in the same axis of the wave propagation. From Campanella's book [3], original title

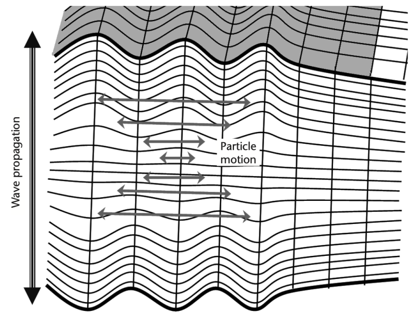

Figure 2.2: Shear or transverse-mode waves: the bulk particles oscillate in the plane perpendicular to the wave propagation and energy transfer. From Campanella's book [3], original title

2.1.2 Fundamentals of the Piezoelectric effect

This section is based on the chapter *2.2.1-Theory of Piezoelectricity* of Campanella's book [3].

Piezoelectric Crystals and References Systems

The piezoelectric effect is a capacity of some material to deform under an electrical excitation. Most of the piezoelectric materials are asymmetric and polarized crystalline structures. Thus, an external electric field will generate opposite forces onto positive and negative poles of the unit cells of the crystal lattice which lead to its deformation.

The application of a stress on the material lattice changes the distance between the positive and negative poles. Subsequently, a net electric field is generated.
Since all material properties of such crystals are anisotropic, they are express as tensors. Furthermore, we need to define a proper reference system.

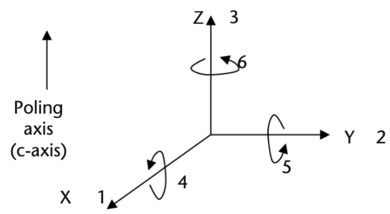

Figure 2.3: Axes convention and directions of deformation. From Campanella's book [3], original title

NOTE: In most simulations (as it is the case in this work), the reference system of the piezoelectric material does not match the geometrical axes.

Using the axis notation defined in the figure 2.3, we can identify constants using two subscripts: the first one describes the direction of the excitation, the second the direction of the response.

Thus, we write 1, 2, 3 the direction X, Y, Z and 4, 5, 6 the shear along these directions.
NOTE : These subscripts can relate either to mechanical or electrical quantity depending of the piezoelectric effect in action (direct or inverse).

Expression of the Piezoelectric Effect

Since the electromagnetic dynamic is faster than the propagation of the acoustic waves, we can describe the relation between mechanics and electromagnetism using a quasi-electrostatic approximation.
Furthermore, if we neglect the magnetic effects, a simple relation between the electric field and applied mechanical stress can be found:

- **Stress-Charge Form:**

$$\begin{aligned} T_{6\times1} &= c^E_{6\times6} \cdot S_{6\times1} - e^E_{6\times3} \cdot E_{3\times1} \\ D_{3\times1} &= e_{3\times6} \cdot S_{6\times1} - \epsilon^S_{3\times3} \cdot E_{3\times1} \end{aligned} \tag{2.1}$$

Where T is the stress matrix, c is the stiffness matrix, S is the strain matrix, e the piezoelectric constant matrix, E is the electric field D the electric density displacement matrix, and ϵ the permittivity matrix. We use the super-indices on ϵ and c to highlight that their are evaluated at constant strain and electric field respectively.
NOTE: In that special case, the subscripts refer to the dimension of the tensors.

Depending of the boundary conditions, this constitutive equation may be quite complicated to solve. This is why alternative forms has been derived:

- **Stress-Voltage Form:**

$$\begin{aligned} T_{6\times1} &= c^D_{6\times6} \cdot S_{6\times1} - h_{6\times3} \cdot D_{3\times1} \\ E_{3\times1} &= -h_{3\times6} \cdot S_{6\times1} - \beta^S_{3\times3} \cdot D_{3\times1} \end{aligned} \tag{2.2}$$

- **Strain-Charge Form:**

$$\begin{aligned} S_{6\times1} &= s^E_{6\times6} \cdot T_{6\times1} + d_{6\times3} \cdot E_{3\times1} \\ D_{3\times1} &= d_{3\times6} \cdot T_{6\times1} + \epsilon^T_{3\times3} \cdot E_{3\times1} \end{aligned} \tag{2.3}$$

- **Strain-Voltage Form:**

$$\begin{aligned} S_{6\times1} &= s^D_{6\times6} \cdot T_{6\times1} + g_{6\times3} \cdot D_{3\times1} \\ E_{3\times1} &= -g_{3\times6} \cdot T_{6\times1} + \beta^T_{3\times3} \cdot D_{3\times1} \end{aligned} \tag{2.4}$$

Where s is the compliance matrix, β the inverse of the permittivity matrix, and d, g and h are the alternative piezoelectric coefficients matrices.

2.1.3 AlN and AlScN as Piezoelectric Material

Assets of AlN/AlScN Thin Films

Just like magnetic materials, piezoelectric materials are characterized by a Curie temperature above which they lost their piezoelectric properties. Traditional piezoelectric materials such as Zinc Oxide (ZnO) and Barium Titanate (BaTiO3) are thus limited to $400-450$ $[K]$ which is not enough for harsh environment sensing and aerospace industry. However, they demonstrate a high electromechanical coupling coefficients. Indeed, Zhang and al. [4] have identified an inverse relationship between Curie temperature and the coupling coefficient.
AlScN became quite popular the last few years since it seems to be today's best compromise [5], combining the high temperature capabilities of AlN[1] with high coupling coefficients.
Lozzi and al. [6] also demonstrated that the 1/F noise of resonators based on AlScN thin films is lower than when using AlN.

Annealing of AlN/AlScN Thin Films

As mentioned before, AlN is quite adapted for high temperature environment. According to the study of Hong and al.[7], the performances of an AlN/Si SAW resonator are not significantly deteriorated after 30min of thermal annealing at $900°C$.
In their analogue study, Aubert and al. [8] have noticed a significant increase of insertion lost after a 30min-annealing at $950°C$. This result was attributed to the degradation of the electrodes' conductivity under oxidation. . However, it is a good illustration of the challenges to tackle to achieved the physical limit of AlN (i.e. 1150 $[°C]$).
NOTE: Solving this issue is out of the scope of this work but few easy solutions may be implemented such as using Molybdenum instead of Platinium or passivate the surface.

Temperature shift of AlN/AlScN based resonators

Aubert and al. [9] have recorded the resonance frequency of an AlN/Sapphire based SAW delay line for a ramp of temperature from 20 to $1050°C$. Their results show a quasi linear variation of the resonance frequency on the full range of temperature (Temperature Coefficient of Frequency: $TCF_{1st\ order} = -71\ [ppm \cdot K^{-1}]$ and $TCF_{2nd\ order} - 12\ [ppb \cdot K^{-2}]$).
Similar results were found for AlSc(0.10)N by Bartoli and al. [10] ($T = [0-500]\ [°C]$, $TCF_{1st\ order} = -67\ [ppm \cdot K^{-1} is]$) and for Lamb wave resonators by Chih Ming and al. [11] ($T = [0-500]\ [°C]$, $TCF_{1st\ order} = -28.14\ [ppm \cdot K^{-1}]$ and $TCF_{2nd\ order} - 9.62\ [ppb \cdot K^{-2}]$).
NOTE: It seems that even if both SAW and Lamb wave resonator demonstrated a similar linear behavior, the absolute value of the first order TCF is different. Therefore, an additional study should be conducted to characterise the temperature behaviour of SAW/BAW (Bulk Acoustic Wave) hybrid resonators.

[1] AlN exhibits piezoactive behavior up to 1150 $[°C]$)

2.2 Acoustic Micro-Resonators

2.2.1 Resonators Performance Monitoring

This section presents the few variables we monitor to evaluate the performances of our device.

Resonance frequencies

Only a limited number of frequency are solution to the wave equation for a resonator. They are identified as resonance frequencies.
In the context of acoustic resonators, the IEEE Std 176-1987 [12] identifies two remarkable frequencies associated to a resonant mode:

- **Series Resonant Frequency:** Written f_s, the series resonant frequency is the frequency where the impedance of the device is the lowest.
- **Parallel Resonant Frequency:** Written f_p, the parallel resonant frequency is the frequency where the impedance of the device is the highest.

The material damping results in the imaginary nature of a resonator response. However, for low isotropic damping coefficients, the *real* resonance frequency is quite close to the parallel resonant frequency. In this report, we will make the approximation that there are identical: $f_{res} \equiv f_p$. We may use either f_{res} or f_p depending of the context.

Note on allowed bandwidth in aerospace

The bandwidth allocation in the aerospace industry is quite restrictive. Gao and al. [13] identify only three bandwidths available for Airborne Wireless Sensors Networks (AWSN): L-Band from 1350 to 1400 $[MHz]$, S-Band from 2.2 to 3.4 $[GHz]$ and S-Band from 4.2 to 4.4 $[GHz]$. We will focus on the first S-Band with a primary objective at $2.45[GHz]$

Electromechanical Coupling Factor

The electromechanical coupling factor is an indicator which quantify the efficiency of the energy conversion between mechanical and electrical. From Uchino's book [14]:

$$\begin{gathered}\frac{Stored\ Mechanical\ Energy}{Input\ Electrical\ Energy}\\ OR\\ \frac{Stored\ Electrical\ Energy}{Input\ Mechanical\ Energy}\end{gathered} \tag{2.5}$$

We can measure its value from the impedance of the system. The following relation links the resonant frequencies to the electromechanical coupling factor (see [15]):

$$k_t^2 = (\frac{\pi}{2})\frac{f_s}{f_p}\tan(\frac{\pi}{2}\frac{f_p - f_s}{f_p}) \tag{2.6}$$

For small coupling values, it can be approximated by :

$$k_t^2 = \frac{\pi^2}{4}\frac{f_s \cdot (f_p - f_s)}{f_p^2} \tag{2.7}$$

As the equation 2.7 suggests, the electromechanical coupling factor represents the distance between the parallel and series resonant frequency. At the same time, it determines the operational bandwidth when the resonator is used as filter.

Quality Factor

The quality factor represents the interaction of a resonator with its environment as well as its internal losses. It can be defined as the ratio between the stored energy and the amount of energy lost per cycle [16]:

$$Q = 2\pi \frac{E_{stored}}{E_{lost}} \tag{2.8}$$

Depending of the available data, there are multiple ways to measure the quality factor:

$$Q = \frac{\omega_r}{FWHM} = \frac{S_{21}(\omega_r)}{S_{21}(\omega = 0)} \tag{2.9}$$

Where ω_r is the resonance frequency, $FWHM$ is the Full Width at Half Maximum of the transfer function's resonance peak and S_{21} is the transmission S-parameter.
In this report, all simulated quality factors are directly extracted from COMSOL Multiphysics (`solid.Q_freq`).

Figure of Merit

A Figure of Merit is a variable that is used to quantify the quality of a device, method or in that case acoustic resonator. It allows to compare the utility of various designs even if the underlying mechanisms are different.
Consequently, both k_t^2 and Q can be qualified of FoM. However, for sake of clarity, we will only refer to FoM for the product:

$$FoM = k_t^2 \cdot Q \; [-] \tag{2.10}$$

2.2.2 Surface Acoustic Wave Resonators

Historical Considerations

As presented in Priya's review paper [17], the prediction of SAW by Rayleigh can be traced back to 1885. Such waves propagate along the surface of a solid and are characterized by an exponential decay within depth. They became popular in 1965 with the invention of the InterDigital Transducer (IDT) by White and Voltmer [18]. From temperature sensors to telecommunication filters, in less than 50 years, SAW devices has demonstrated a quite diversified range of application.
As proposed by Schmidt in 1994 [19] and Reindl in 1996 [20], one of the main advantage of SAW devices is it simple remote operation. Indeed, the physical principle of SAW makes it the perfect sensor for harsh environments: by connecting the IDT to an antenna, the wave can be excited using an electromagnetic waves and removes the need for sensible elements such as batteries.

Rayleigh Waves

Rayleigh's waves are the mechanism of the fundamental mode of many SAW devices. As the figure 2.4 suggests, particles at the surface of an isotropic material follow an ellipse. This ellipse is contained in a plane normal at the surface and is orthogonal to the propagation vector.

While going deeper in the material, we observe a succession of retrograde and progressive ellipses. The amplitude of this displacement decreases within the depth of the material and can be approximated as null under one or two times the wavelength.

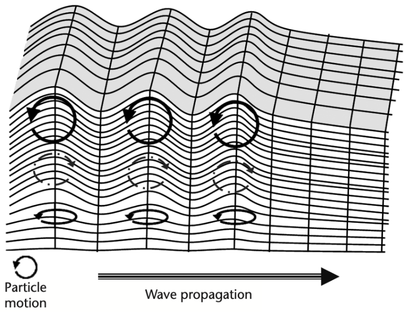

Figure 2.4: Rayleigh wave propagation: the surface particles of an isotropic solid move in ellipses in planes normal to the surface and parallel to the wave direction. From Campanella's book [3], original title

Approximation of Rayleigh Waves velocity

Rahman and al. proposed in 2006 [18] a simple approximation for Rayleigh waves' velocity:

$$c_{Rayleigh} \approx \sqrt{\frac{\mu}{\rho}} \cdot \frac{0.87 + 1.12\nu}{1+\nu} \tag{2.11}$$

Where μ is the second Lamé parameter, ρ is the material density and ν is its Poisson ratio. With this formula, deriving the fundamental resonance frequency from material properties become trivial. It allowed us to free ourselves from the need of eigenfrequency simulation during preliminary studies.

SAW sensors configurations

We can sort SAW sensors based on its ports configuration and the recorded information [3].

- **One-port vs two-ports configurations:** A one-port configuration (see fig. 2.5), both the excitation of the SAW (IN) and the emission of the information (OUT) is done by the same IDT. A two-ports configuration (see fig. 2.5), however, these functions are uncoupled and two IDTs are needed.
- **Standing waves vs delay lines :** Both configurations exploit the same effect: the wave's velocity of the SAW varies according to the physical property we want to measure (temperature, strain, chemical compounds etc). In the standing waves configuration (see fig. 2.5), we confine the wave around the IDT and record the shift of the resonance frequency (we measure a spectrum in $[Hz]$). On the other hand, delay lines (see fig. 2.5) use the propagation of the wave in the material. Multiple markers (Reflectors or secondary IDTs) send back pings which allow to derives the SAW's velocity (we measure a delay in $[s]$) (see fig. 2.5).

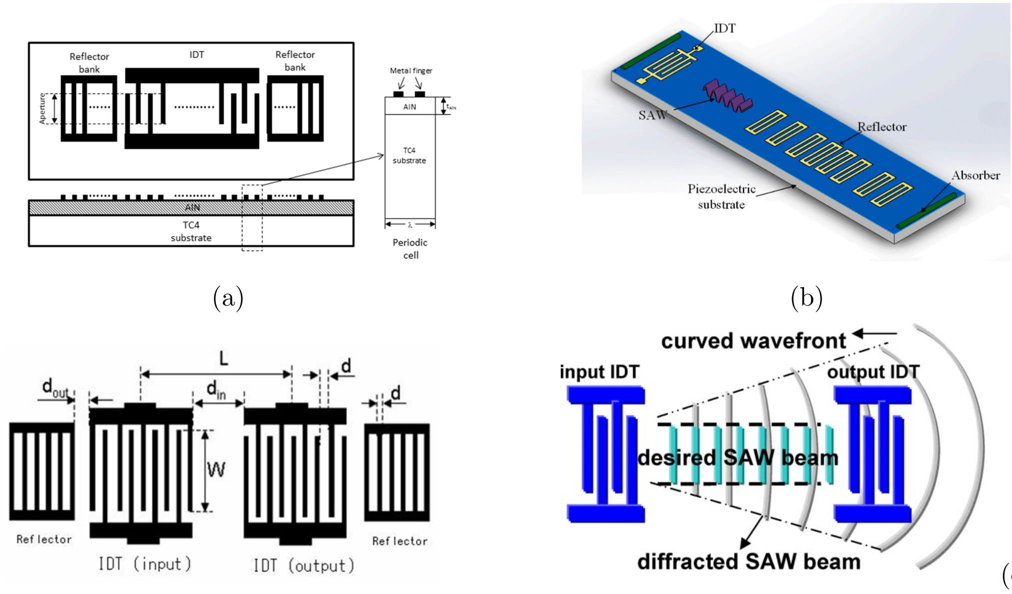

(a) (b) (c) (d)

Figure 2.5: Illustration of SAW sensors configurations. a) Schematics of SAW sensor within a one-port, standing wave configuration (from Shu's paper [21], original title: " Schematic illustration of the one-port surface acoustic wave (SAW) resonator and the Figure 1. Schematic illustration of the one-port surface acoustic wave (SAW) resonator and the modeling periodic cell.") b) Schematics diagram of SAW sensor within a one-port, delay-line configuration (from Fu's paper [22], original title: " Schematic diagram of the wireless and passive SAW temperature sensor.") c) Schematics diagram of SAW sensor within a two-port, standing wave configuration (from Hong's paper [7], original title: " IDT pattern schematics of two ports SAW resonator: a) top view b) cross section") d) Schematics diagram of SAW sensor within a two-ports, delay-line configuration (from Tigli's paper [23], original title: " SAW diffraction problem due to finite aperture.")

AlN/AlScN based SAW Resonator Performances

AlN based SAW resonators has demonstrated a particular high FoM at high frequency (i.e. $k_t^2 \cdot Q = 5.4$ $[-]$ at 3.648 $[Ghz]$ [1]). Moreover, multiple studies has also shown that the piezoelectric response can be enhanced by doping the AlN with Scandium : Ansary and al. [24] experimental results reach $k_t^2 = 3.7[\%]$ with an AlSc(0.12)N SAW device on Si. Wang and al. conducted a similar study [25] and shown an increase of 300% of the coupling efficiency when doping AlN with 27% Scandium.

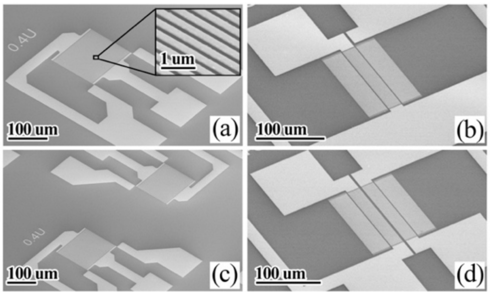

Figure 2.6: SEM Image of AlScN based SAW Resonators. From Hao's paper [1], original title: "SEM images of the fabricated devices: (a) one-port; (b) one-port with reflector; (c) two-port; (d) two-port with reflector"

SAW resonator with Metallic Substrates

While dealing with harsh environment, one common issue is the integration of the sensor. Indeed most of sensors are either glued or screwed. It is not simple to find a glue which sustain 1100 $[K]$ moreover the high creeping and acceleration environment in turbines may lead to premature fatigue for most of mechanical assemblies. To tackle the problem of integration, Shu and al. have studied using titanium alloys as substrate [21]. Even if the coupling efficiency is lower than substrates with high wave velocity such as Single Crystal Diamond (SCD) or Silicon Carbide (SiC), they shown its feasibility. On the long term, they proposed to incorporate SAW devices within functional parts by depositing the piezoelectric layer directly on Ti structures.

2.2.3 Cross-sectional-Lamé-Mode resonators

Combining the e_{31} and e_{33} piezoelectric coefficients, Cross-sectional-Lamé-Mode resonators (CLMRs) transduce a longitudinal vibration mode along both the thickness and the width of a suspended piezoelectric layer. Cassella and al. [26] have studied the behavior and performances of Cross-Sectional-Lamé-Mode in AlN thin film and enabled the excitation of CLMR's modes with high FoM (experimental results: $k_t^2 = 2.5$ $[\%]$ and $Q = 1850$ $[-]$).

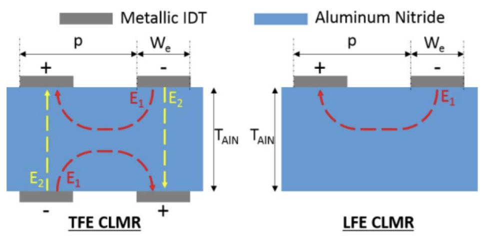

Figure 2.7: Schematics diagram of CLMR resonator. From Cassella's paper [26], original title: "Left: Thickness-Field-Excitation CLMR. $[\cdots]$ Right: Lateral-Field-Excitation CLMR. $[\cdots]$"

2.2.4 Bulk Acoustic Wave resonators

BAW resonators transduce longitudinal acoustic waves within the thickness of the piezoelectric layer. We distinguish two main categories of BAW devices based on the mechanism used to trap the mode in the piezoelectric layer. Film Bulk Acoustic Resonators (FBARs) are suspended structures, the interface air-piezoelectric acts like an acoustic reflector. Solidly Mounted Resonators (SMR) are not suspended, but a Bragg reflector is used at the interface between the bottom electrode and the substrate [27]. Shealy and al. [28] developed an AlN FBAR for multi-GHz filters (3.8 $[GHz]$) with astonishing results (experimental results: $k_t^2 = 5.87$ [%] and $Q = 1572$ $[-]$).

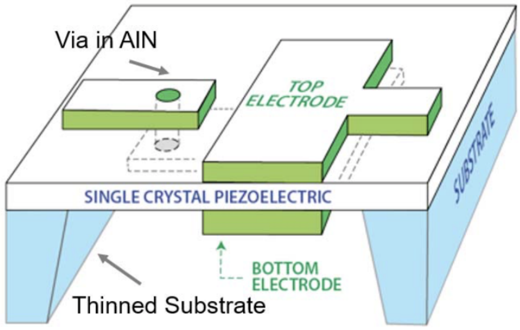

Figure 2.8: Schematics diagram of BAW sensor. From Shealy's paper [28], original title: " A schematic diagram of structure of the fabricated resonators, showing top and bottom electrodes on single crystal AlN and a via in AlN to connect to the bottom electrode, situated inside a cavity in a thinned SiC substrate."

2.2.5 SAW-BAW hybrid resonators

In 2016 and 2017, Paschenko and al. [29][30] proposed the design of a *3d Type FBAR*. They created an array of Al-N/AlScN pillars spaced by a distance $pitch = \lambda_{SAW}/2$. These pillars are actuated as an array of BAW resonators where two consecutive resonators have opposite phases.

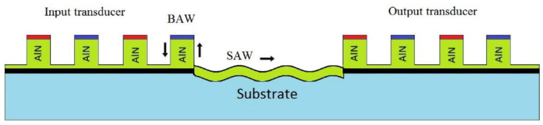

Figure 2.9: Schematics diagram of SAW-BAW hybrid sensor. From Pashchenko's paper [29], original title: "Delay line design with hybrid BAW/SAW transducer"

Thanks to a coupling between the BAW array and the substrate, they are able to excite a SAW mode along the remaining piezo-electric layer. They found an optimal transformation of BAW to SAW when $t_{piezo} = \lambda_{SAW}/2$ or $t_{piezo} = \lambda_{SAW}/4$. Their experimental results on sapphire substrate reveal a good electromechanical coupling at low frequency (i.e $f_{res} = NA$ $[MHz]$; $k_t^2 = 0.6$ [%] for AlN and $f_{res} = 613$ $[MHz]$; $k_t^2 = 3.8$ [%] for AlSc(0.15)N) but they recorded a low Q-factor which lead to a lower FoM than previously mentioned resonators.

Chapter 3

Simulation - Unity Cell

3.1 Simulation Setup

3.1.1 Procedure

The Finite Element Method (FEM) simulations presented in this report have been conducted using COMSOL Multiphysics and its official package LiveLink™for MATLAB®. Since such packages are not widely used, we dedicated this section to the procedure we used. According to the official *LiveLink™for MATLAB®*'s user's guide, this package allows to:

> *LiveLink™for MATLAB® connects COMSOL Multiphysics to the MATLAB scripting environment. Using this functionality you can do the following:*
>
> - *Set Up Models from a Script [...]*
> - *Use MATLAB Functions in Model Settings [...]*
> - *Leverage MATLAB Functionality for Program Flow [...]*
> - *Use MATLAB Functions in Model Settings [...]*
> - *Create Custom Interfaces for Models [...]*
> - *Connect to COMSOL Server™*

Geometry definition and parametrization

Since the geometry of the unit cell is quite simple, we decided to build it directly in COMSOL's Graphical User Interface (GUI). We also declare global parameters and used them to fully parametrize the geometry.

Materials allocation

In COMSOL's GUI, we created material sweeps for the substrate, the piezo-electric layer and the electrodes. Using material sweeps is quite interesting while conducting parametric study. Indeed, the materials can be easily (dis/en)abled without interfering with the rest of the setup.

Since the environment do not change in this study, we do not used material sweep for the air domains.

Boundary conditions definition

In COMSOL's GUI, we applied all the boundary (and domains) conditions as it is usually done in COMSOL without LiveLink™package.

Mesh generation

The mesh has been traditionally defined directly in COMSOL's GUI. Note that the elements' distribution is done in function of the geometry parameters to ensure convergence with all design points.

Connect MATLAB to COMSOL Server™

Once the initial setup is ready, we launch LiveLink™for MATLAB® which connect a MATLAB session to COMSOL Server™. We are then able to open, through MATLAB our COMSOL model (.mph) in COMSOL Server™.

Run the Simulation

We can then pilot COMSOL from MATLAB. Indeed, a pointer to the model is created while loading the .mph file. It can be used to perform any action available in COMSOL environment : (dis/en)able materials, (dis/en)able boundary conditions, change global parameters, set solvers parameters, run simulations. LiveLink™for MATLAB® allows to reduce drastically the computation time by coupling multiple studies and pre/post-processing:

- **Eigenfrequency study:** the resonance frequency of the first SAW/BAW mode is determined by the geometry of the device and the materials used. For the considered designs set, it varies from 600 $[MHz]$ to > 3.2 $[GHz]$. If we want to have at least 5 points between the parallel and series resonance peaks, we must compute a total of 15'000 frequencies on the full bandwidth[1]. Therefore, we identify, through this eigenfrequency study, the resonance frequency of the fundamental SAW/BAW mode in order to narrow the frequency range in the next study.
  NOTE: In this report, the mode identification is done manually but it may be automatized in the future. Indeed, an algorithm with a 90% success rate has been developed. We are quite confident that the required objective of 100% can be reached with some more research.

- **Frequency Domain study 1:** This first frequency domain study aims to compute the frequency response of the devices' admittance around its identified resonance frequency. We compute between 400 and 1000 points (bandwidth: $[f_{res} - 100MHz; f_{res} + 500MHz]$)

[1]Considering the lowest coupling factor is $k_t^2 = 0.2\%$ at $1GHz$.

depending of the materials[2]. As presented in the figure 3.1, for some designs, the first mode disappears when the material damping is enabled: the studied mode is nonexistent for those designs. To allow an automatic identification of k_t^2 during the post-processing step, we cancel those exceptions by disabling the material damping.

- **Post-processing 1:** We extract from the devices's admittance the resonance and anti-resonance frequencies.
- **Frequency Domain study 2:** This second frequency domain study aims to extract the quality factor. Thus, we activate material damping and compute 3 points centered on the resonance frequency.
- **Post-processing 2:** Once both k_t^2 and Q are defined, we need to process the exceptions ignored during the first frequency domain study. We considered that the mode is nonexistent if the FWHM of the resonance peak is larger than the difference between resonance and anti-resonance frequencies :

$$k_t^2 \leftarrow 0 \; if \; \Delta f < \frac{2 * \pi * f_{res}}{Q} \tag{3.1}$$

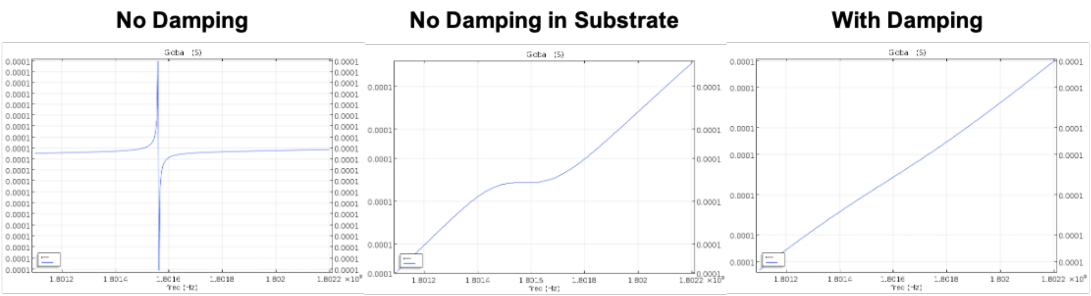

Figure 3.1: Mode extinction caused by material damping in AlN SAW/BAW hybrid resonator. Simulation parameters : $pitch = 1.0$ $[\mu m]$; $etching\ depth = 05$ [%]; $t_{AlN} = 0.3$ $[\mu m]$; $t_{Pt} = 50$ $[nm]$; $coverage = 50$ [%]; Substrate=Si

[2] A preliminary study has given an a priory coupling efficiencies which allow us to estimate $\Delta f = f_p - f_s$. To save time, we lower the number of points for materials with high coupling efficiency

3.1.2 Geometry Definition

The geometry of the unity cell is presented in figure 3.2. We placed the origin of the geometrical axis (X pointing to the right, Y pointing up and Z pointing in the plane) on the left side of the geometry at the interface between the bottom electrode and piezoelectric layer.
The parameters and their descriptions are presented in the table 3.1. With the following definitions, they fully constrain the geometry:

- The in-plane depth is fixed to $50\mu m$
- In traditional SAW device, the displacement's intensity decrease exponentially along geometrical -Y axis. Thus, we made the assumption that, for the mode of interest, nothing happens in the substrate under two times the wavelength. Thus, we created a substrate's layer with a thickness of 3 λ_{SAW} ($6 \cdot pitch$) which includes a $2 \cdot pitch$-square Perfectly Matched Layer (PML).

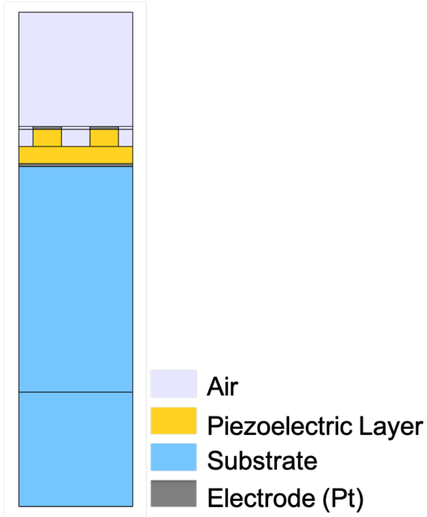

Figure 3.2: Geometry and material domains of unity cell. Figure parameters : $pitch = 1.0$ $[\mu m]$; $etching\ depth = 50$ [%]; $t_{AlN} = 0.6$ $[\mu m]$; $t_{Pt} = 50$ $[nm]$; $coverage = 50$ [%]

- The center of the top electrodes are placed at $Y = +pitch/2$ and $Y = +3 \cdot pitch/2$.
- The thicknesses of the top and bottom electrodes are identical.
- The top domain (Air) is a square with a side equal to $2 \cdot pitch$.

NOTE: The SAW's fundamental mode wavelenght is equal to twice the pitch of the device: $\lambda_{SAW,fundamental} = 2 \cdot pitch$.

We selected Ti for the electrodes because of its high melting point (≈ 1700 $[°C]$). All material properties were imported from COMSOL's library but AlSc(0.17)N and AlSc(0.40)N which are described in the appendix A.

Parameter	Unit	Definition
pitch	$[\mu m]$	Half width of the unity cell / Distance between two consecutive electrodes
etching depth	$[\%]$	Ratio between the piezo-electric layer thickness and the etching depth (trenches depth)
coverage	$[\%]$	Top electrode coverage : Metalisation ratio of top electrode $(electrode\ surface/total\ surface)$
t_{piezo}	$[\mu m]$	Piezoelectric layer's thickness. To prevent confusion, *piezo* is replaced by the considered piezoelectric material : AlN, $AlSc(0,.17)N$ or $AlSc(0.40)N$
t_{IDT}	$[nm]$	Electrodes' thickness [3]

Table 3.1: Definition and Units of Considered Parameters

3.1.3 Environment Definition

Mechanics Environment

The mechanical environment is defined for all domains excepts the domains with air. We used a plane strain 2D approximation with the out-of-plane mode extension enabled (out-of-plane wave number $k_Z = 0\ [rad \cdot s^{-1}]$). The figure 3.3 shows the main conditions declared in the simulation. The full description is presented in the Appendix B, table B.1.

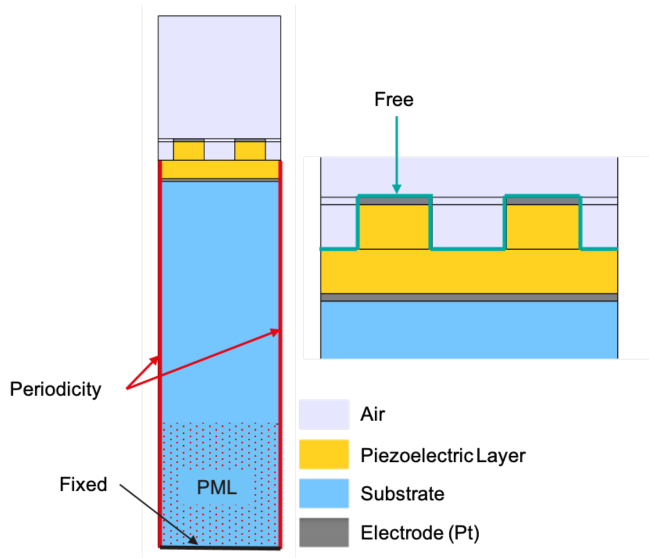

Figure 3.3: Main mechanical boundary conditions for the unity cell simulation. Figure parameters : $pitch = 1.0\ [\mu m]$; $etching\ depth = 50\ [\%]$; $t_{AlN} = 0.6\ [\mu m]$; $t_{Pt} = 50\ [nm]$; $coverage = 50\ [\%]$

Electrostatics Environment

The electrostatic environment is defined for all domains excepts the PML. We consider a non-nul out-of-plane thickness and a reference impedance, $Z_{ref} = 50$ $[\Omega]$. The figure 3.4 shows the main conditions declared in the simulation. The full description is presented in the Appendix B, table B.2.

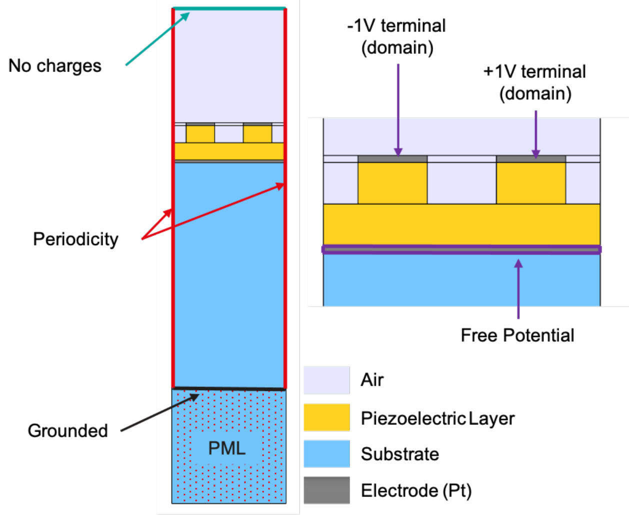

Figure 3.4: Electrostatic boundary conditions setup for the unity cell simulation. Figure parameters : $pitch$ = 1.0 $[\mu m]$; $etching\ depth = 50$ [%]; $t_{AlN} = 0.6$ $[\mu m]$; $t_{Pt} = 50$ $[nm]$; $coverage = 50$ [%]

Multiphysics Environment

Only one condition is defined in the Multiphysics environment : the piezoelectric effect 1. Applied to the piezoelectric layer, it couples the solid mechanics and electrostatic environments.

3.1.4 Mesh Definition

The mesh is the most critical element of a piezoelectric multiphysic simulation. We need thus to fully control the mesh:

- We first defined the left vertical edge.
  - The smallest layers are the two metallic domains. We impose thus a homogeneous distribution containing 2 elements on these two segments.

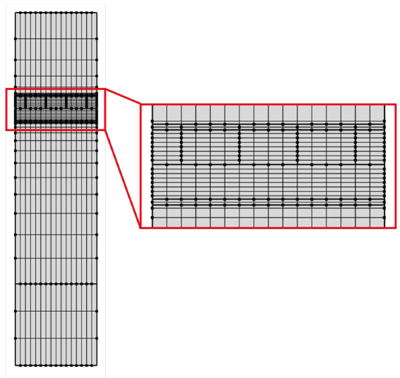

Figure 3.5: Typical aspect of build mesh. Figure parameters : $pitch = 1.0$ [μm]; $etching\ depth = 50$ [%]; $t_{AlN} = 0.6$ [μm]; $t_{Pt} = 50$ [nm]; $coverage = 50$ [%]; $X_{piezo} = 15$; $X_{substrate,air} = 5$

  - Then we impose homogeneous distributions on the piezo electric layer. The number of elements is allocated between the two segments following the rules :

$$N_{piezo,1} = max(ceil(X_{piezo} \cdot (etching\ depth))\ ,\ 2) \tag{3.2}$$

    where the piezoelectric layer is etched and:

$$N_{piezo,1} = max(ceil(X_{piezo} \cdot (1 - etching\ depth))\ ,\ 2) \tag{3.3}$$

    where it is still intact.
  - For the air and substrate layers, we decided to use a geometric distribution to match the mesh size at their interface with the metal layers. The geometric modulus has been computed as follow:

$$\begin{aligned} R_{substrate} &= abs((8 \cdot pitch/X_{substrate,air}) - 3 * S)/S \\ R_{air} &= abs((4 \cdot pitch/X_{substrate,air}) - 3 * S)/S \end{aligned} \tag{3.4}$$

    Where $S = t_{IDT}/2$.
  - We used a homogenous distribution for the PML. The number of elements has been selected to best match the lower element of the substrate:

$$N_{PML} = floor(2 \cdot pitch/(S * R_{substrate})) \tag{3.5}$$

- The next step is to copy this edge onto the right vertical edge to ensure the validity of the periodicity conditions. We also copy the corresponding edges onto undefined vertical segments.

- We then distributed a total of 16 elements on the horizontal edges according to the value of *coverage*:

$$N_{IDT} = ceil(16 * (coverage)/2) \tag{3.6}$$

- Once all edges are sliced, we map all domains to obtain the mesh as presented in figure 3.5.

During the setup of the mesh, we noticed small variations of the series and parallel resonant frequencies. Knowing that a small difference of $+/-1\%$ on those frequencies may lead to a 25% variation of the electro-mechanical coupling[4]. A convergence study were thus mandatory to ensure the validation of our study. We used two parameters, $X_{substrate,air}$ and X_{piezo}, to parametrize the number of elements on the vertical edge.

The figure 3.6 presents the evolution of f_p, f_s as well as the computation time computed during the sweep of this two parameters (from 2 to 30 for X_{piezo} and from 2 to 10 for $X_{substrate,air}$). Both frequencies seems to stabilize for $X_{piezo} >= 12$ and $X_{substrate,air} >= 3$. To take in account this convergence may differ slightly with a different design, we decide to take some margin within keeping a reasonable computation time. We choose thus $X_{piezo} = 15$ and $X_{substrate,air} = 5$ (computation time for 2500 points: $t_{comp} = 359.7[s] \implies \approx 7pts/s$)

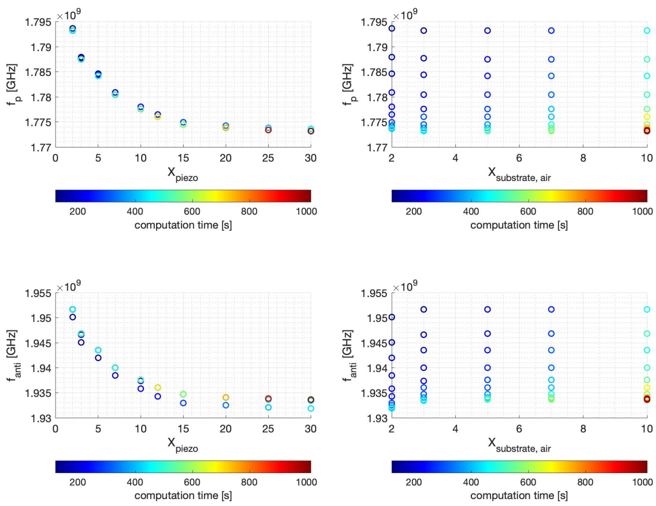

Figure 3.6: Variation of the parallel resonant frequency, f_p, series resonant frequencies, f_s, and computation time during the UC simulation in function of the number of elements in the piezoelectric and substrate/air domains. Simulation parameters : $pitch = 1.0\ [\mu m]$; $etching\ depth = 50\ [\%]$; $t_{AlN} = 0.6\ [\mu m]$; $t_{Pt} = 50\ [nm]$; $coverage = 50\ [\%]$; Piezoelectric layer= AlSc(0.40)N; Substrate: SCD; Number of frequency: 2500

[4]If we consider the two extreme cases of the convergence study we have conducted (i.e. $f_{res} = 1.01 \cdot 1.774[GHz] = 1.794[GHz]$ and $f_{anti} = 0.99 \cdot 1.952[GHz] = 1.934[GHz]$) the variation in k_t^2 is as high as 23.4% ($0.1657[-]$ vs $0.2045[-]$). Since both f_p and f_s decrease while X_{piezo} increases, the actual maximum variation of k_t^2 observed is close to 3.1% ($0.1821[-]$ vs $0.1877[-]$)

3.1.5 Setup Validation

Once the simulation is ready, we used the experimental results of Hao and al. [1] to validate our setup and mesh.
Some minor adjustments are required to match Hao's device. Thus, we align our parameters to their geometry (see table 3.2). Our parametrization does not allow, *etching depth* to be (close to) zero[5]. However, Hao's device is a pure SAW device. Therefore, we use an *etching depth* value of 50% and applied AlN (and the corresponding mechanical & electrostatic conditions) to the "etched domains". Moreover, they do not have a bottom metallisation. Therefore, we allocate the bottom electrode to the substrate domain and deactivate its floating potential. Finally, we selected gold as electrode material and run the simulation.

The parallel resonant frequency measured by Hao and al. for their AlN based resonators is $f_{p,\ Hao} = 3.992 \pm 0.003\ [GHz]$ depending of SAW configuration (one or two-ports + with-/without reflectors). From our simulation, we find $f_{p,\ valid} = 4.002\ [GHz]$ (see mode shapes in fig. 3.7 and displacements in 3.8).
This results validate our setup since the small variation of 0.25% can be explained by the manufacturing tolerances and the variation of material properties during deposition.

pitch $[\mu m]$	*etching depth* [%]	*coverage* [%]	t_{piezo} $[\mu m]$	t_{Au} $[nm]$	Substrate	Piezoelectric
0.4	50	50	0.4	80	Si	AlN

Table 3.2: Parameters used for the validation of our simulation setup - Based on Hao's Device [1]

[5]We randomly define the minimal value of *etching depth* to 5%.

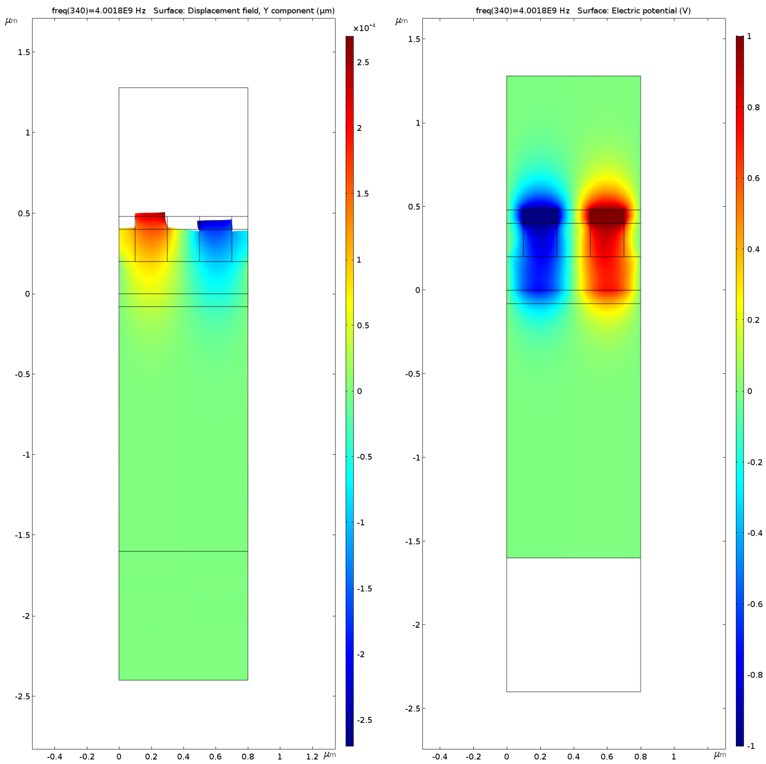

Figure 3.7: Surface Vertical Displacement (Deformation Scale Sactor = 100) and Surface Electric Potential of our Validation Simulation at Resonance Frequency ($f_{res} = 4.0018$ $[GHz]$)

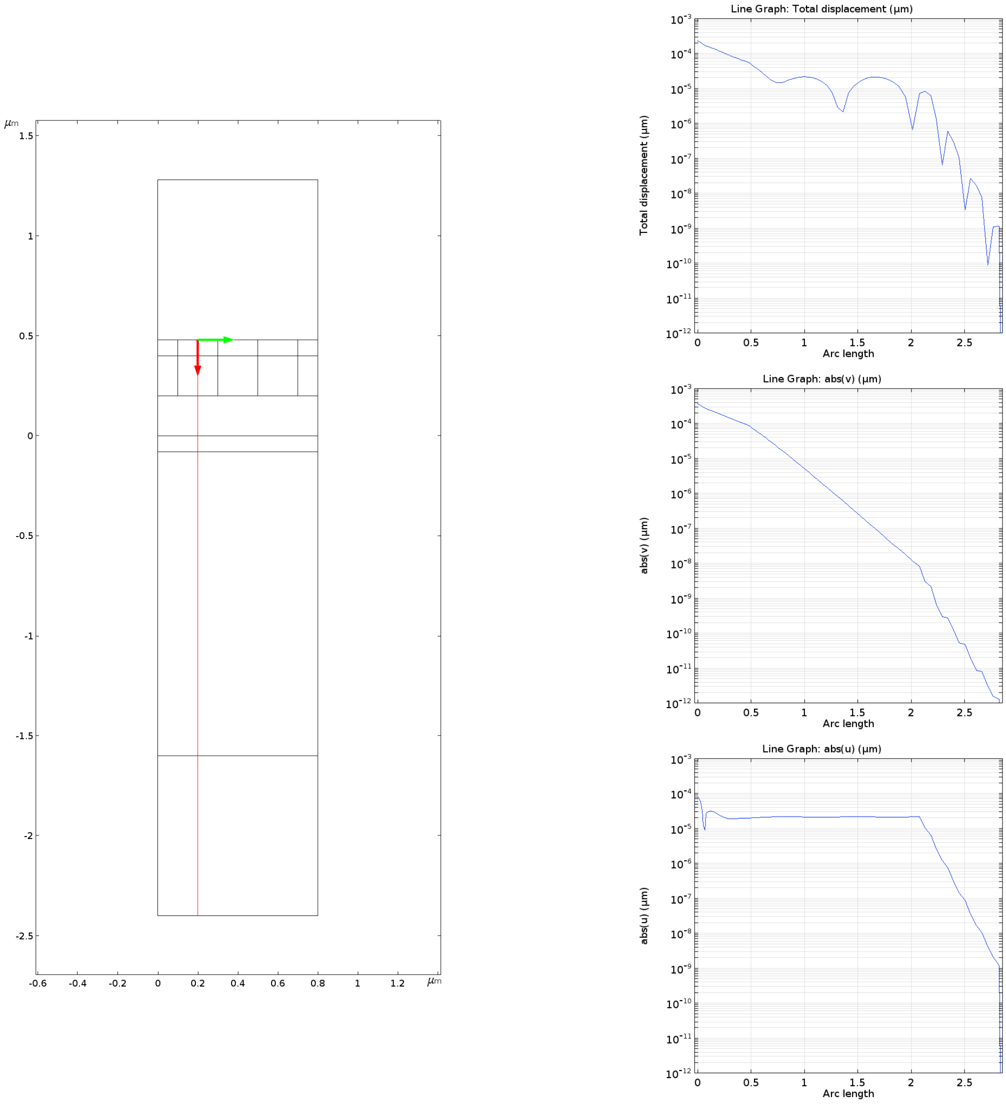

Figure 3.8: Cut-line representation and extracted data (total, vertical & horizontal displacement) of our Validation Simulation at Resonance Frequency ($f_{res} = 4.0018$ $[GHz]$)

3.2 Preliminary Studies

3.2.1 Piezoelectric Coupling Matrix

The first step of this work is to understand the mechanisms occurring in the fundamental SAW response of a AlScN layer.

We run a series of simulations aiming to highlight the main interaction between the electrical and mechanical displacement fields. Therefore, one-by-one, we turned to zero the coefficients of the AlSc(0.40)N coupling matrix and recorded the electromechanical coupling factor into the table 3.3. This interaction is quite obvious since k_t^2 extinguishes only when $d_{33} = 0$ $[C \cdot m^{-2}]$. The main mode of our AlSc(0.40)N device is thus a vertical strain mode which is exited when the electric field is parallel to the geometrical Y-axis.[6]

Virtual alteration of coupling matrix	$k_t^2[\%]$
None	5.698
$d_{15} = 0$ $[C \cdot m^{-2}]$	6.679
$d_{31} = 0$ $[C \cdot m^{-2}]$	6.224
$d_{32} = 0$ $[C \cdot m^{-2}]$	5.641
$d_{33} = 0$ $[C \cdot m^{-2}]$	0.131

Table 3.3: Impact of AlSc(0.4)N's coupling matrix on electro-mechanical coupling (k_t^2)
Simulation parameters : pitch $= 1.0$ $[\mu m]$*; etching depth* $= 00$ $[\%]$*;* $t_{AlSc(0.4)N} = 50$ $[nm]$*;* $t_{Pt} = 50$ $[nm]$*; coverage* $= 50$ $[\%]$*; Substrate=SiC*

NOTE: At the time of this preliminary study, the simulation setup was different that the one presented in the previous sections. It was similar to the one used for validation (see section 3.1.5) but with another combination of materials.

[6]Remember the material Z axis is equivalent to the geometrical Y-axis.

3.2.2 Impact of Substrate Dielectric Constant

Since the preliminary study has shown that the main mode is excited through d_{33}, we search solutions to guide the electric field along the geometrical Y-axis.
One solution is to create a physical path by etching the piezoelectric layer. This solution will be studied in the next sections. First, we study the impact of the substrate's dielectric constant onto the coupling factor. Indeed, if the piezoelectric layer is small relatively to the pitch, the electric field will a priori align itself with the geometrical Y-axis if the substrate's dielectric constant is high.

Thus, we create a virtual substrate material based on SiC: all the material constants are identical except for the dielectric constant which is replaced with a global parameter subject to a parametric sweep.
As shown in the figure 3.9, our hypothesis is confirmed: for thickness-over-pitch ratio bellow 1, the electromechanical coupling increase within the substrate's dielectric constant.
Because of this result, we decided to add a bottom electrode as shown in the figure 3.2. We assume a perfect conduction in the bottom electrode which is simulated with a floating potential imposed at the domain's boundaries.

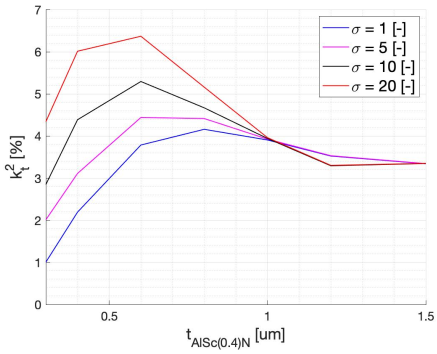

Figure 3.9: Impact of substrate's dielectric constant (σ) onto electromechanical coupling factor(k_t^2) in function of AlSc(0.4)N thickness. Simulation parameters : $pitch = 1.0$ [μm]; $etching\ depth = 05$ [%]; $t_{Pt} = 50$ [nm]; $coverage = 50$ [%]; Substrate=SiC

According to a current study conducted within ANEMS group by Marco Liffredo, fewer abnormal grains are observed during the growth of highly doped AlScN layer on a metallic layer (Pt) than directly on Si. The bottom electrode has thus two functions since it increases both the quality of the piezoelectric layer and channels the electric field.

NOTE: To keep the geometry and mesh constant along the study, the bottom electrode's domain will remains even we consider there is no bottom electrode. In those cases, we only disable the floating potential boundary condition.

3.2.3 Substrate selection

Confinement of the wave into the piezoelectric layer is primordial to achieve high electromechanical coupling efficiency. The literature has widely demonstrated the choice of substrate's material plays a major role in the performances of a SAW resonator. As a large difference in reflective index allows to confine light inside an optical fiber, Hashimoto and al. [31] [32] have shown that substrates with high wave velocity promote the confinement of the SAW and hence increases the performances of the resonator.

In this study, we select three substrates (i.e. SCD, SiC and Si) and compared their performances for different designs. The figures 3.10, 3.11 and 3.12 (AlN, AlSc(0.17)N and AlSc(0.40)N respectively) present the variation of the electro-mechanical coupling factor with the thickness of the piezoelectric layer in the presence of a bottom electrode.

As we expected, the coupling efficiency is much higher for SCD and SiC than for Si. Indeed, the speed velocity of these material is quite high and their isotropic damping factor are lower than Si at the GHz range. The performance of SCD is slightly better than SiC. However, we decided to use SiC in the rest of the study because of it is more available than SCD.

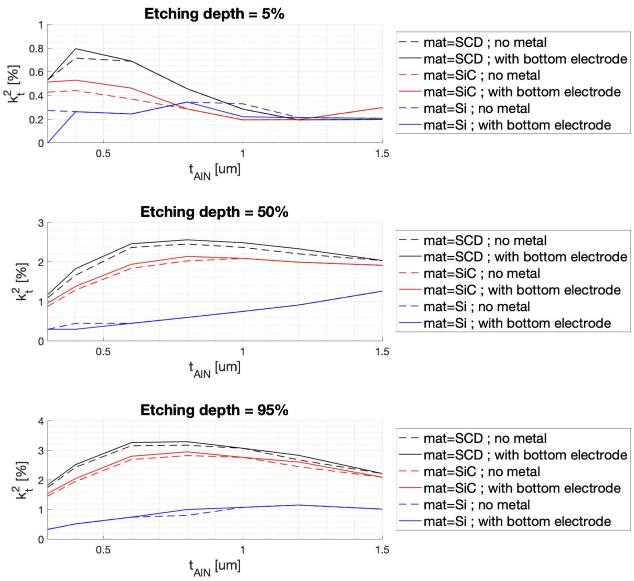

Figure 3.10: Impact of the substrate and bottom electrode onto electro-mechanical coupling (k_t^2) in function of AlN thickness. Simulation parameters : $pitch = 1.0$ [μm]; $t_{Pt} = 50$ [nm]; $coverage = 50$ [%]; Substrate=SiC.

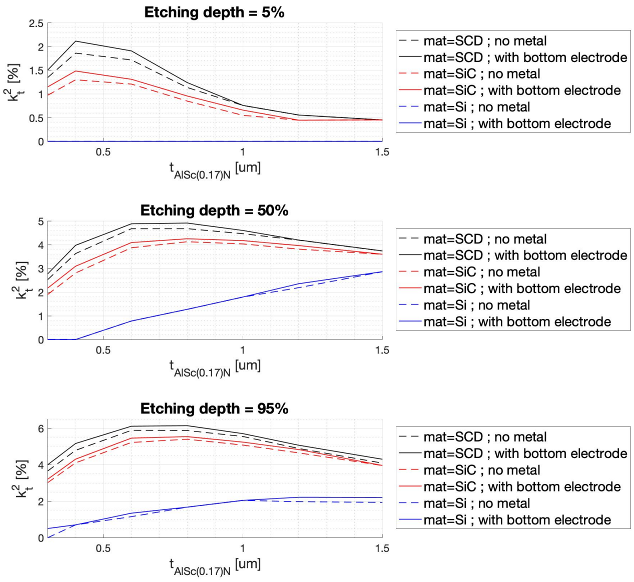

Figure 3.11: Impact of the substrate and bottom electrode onto electro-mechanical coupling (k_t^2) in function of AlSc(0.17)N thickness. Simulation parameters : $pitch = 1.0$ $[\mu m]$; $t_{Pt} = 50$ $[nm]$; $coverage = 50$ [%]; Substrate=SiC.

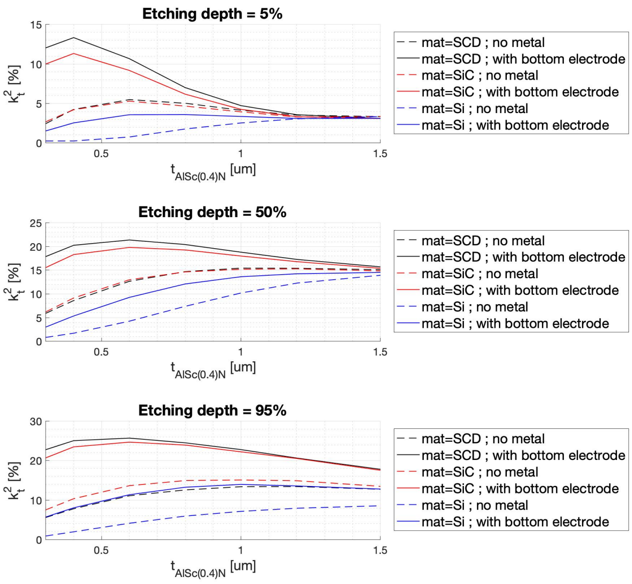

Figure 3.12: Impact of the substrate and bottom electrode onto electro-mechanical coupling (k_t^2) in function of AlSc(0.4)N thickness. Simulation parameters : $pitch = 1.0$ $[\mu m]$; $t_{Pt} = 50$ $[nm]$; $coverage = 50$ [%]; Substrate=SiC

3.3 Parametric Study

3.3.1 Scope

This parametric study aims to determine the relation between the performance of the resonator and its geometry. We generated three different data sets, one for each studied piezoelectric material: AlN, AlSc(0.17)N and AlSc(0.40)N.
A standard analysis containing 324 design points were first been conducted. With these first results, we have noticed that the global trends both in term of performances (i.e. k_t^2, Q) and relative resonance frequency were identical for all considered piezoelectric materials.
Because of the time restriction of the project, we thus decided to run an extended parametric study with 450 design points only for AlSc(0.40). Moreover, we decided to not sweep the IDT's coverage (fixed to 50%). Indeed, this is the parameter with the lowest repeatability during manufacturing and it has the smaller impact on the electromechanical coupling. We sweep thus only 4 parameters in the extended study: it allows to increase their range and limit the total number of design points.
The design sets are composed of each combination of parameters' values presented in the table 3.4.

NOTE: In this report we only present the extended version of the parametric analysis for AlSc(0.4)N.

Parameter	Unit	Values - Initial Study	Values - Extended Study
pitch	$[\mu m]$	$[0.8; 1.0; 1.5]$	$[0.8; 1.0; 1.2; 1.4; 1.6]$
etching depth	[%][7]	$[20; 50; 75]$	$[5; 25; 50; 75; 95]$
coverage	[%]	$[40; 50; 60]$	$[50]$
Piezoelectric layer's thickness	$[\mu m]$	$[0.4; 0.6; 1.0]$	$[0.3; 0.4; 0.6; 0.8; 1.0; 1.5]$
Electrode's thickness [8]	$[nm]$	$[50; 75; 100]$	$[50; 75; 100]$

Table 3.4: Parameters' range considered during the parametric studies

3.3.2 Main Effect Plot

A main effect plot is a statistical tool which allow to study the first order impact of the parameters onto performances. One graph is generated for each parameter. It represents, by a line plot, the mean value of the performance (k_t^2 and Q in our case) in function of the aforementioned parameters.
In the figures 3.13, 3.14 and 3.15, we present the main parameter's effects onto the coupling efficiency and the quality factor for SAW/BAW hybrid devices based on AlN, AlSc(0.17)N and AlSc(0.40)N respectively.

Impact on k_t^2 of

- **the pitch:** A priori, the electromechanical coupling factor seems to be inversely proportional to the pitch. We will show in the section 3.3.3 that this effect is true only for the considered ranges. Indeed, if we consider a second order effect, we realize that multiple maximums exist and there is an interaction between the pitch and the thickness of the piezoelectric layer.
- **the etching depth:** As mentioned previously, etching the piezo electric layer allow us to channel the electric field and thus enhance the electro-mechanical coupling efficiency. We observe a significant increase of k_t^2 (AlN : +204%, AlSc(0.17)N:+107%, AlSc(0.40)N:+265%).
- **the IDT's coverage:** Within the studied design sets, no relation between the IDT's coverage and the coupling efficiency can be identified.
- **the thickness of the piezoelectric layer:** A maximum of the electro-mechanical coupling seems to be achieved for a piezoelectric layer around $0.8 - 1.0[\mu m]$ depending of the piezoelectric material. As we will discuss in the next section, this effect may be biased because of the considered design sets (the ratio $t_{piezo}/pitch$ seems to be more important).
- **the thickness of the metallic layer:** From the simulation, the thickness of the electrodes do not have a huge impact on k_t^2. However, some approximations of the simulation (i.e. perfect conduction) may lead to a different experimental behavior.

Impact on Q of

- **the pitch:** Both parametric simulations (standard and extended) seems to show a local minimum for $pitch = 1$ $[\mu m]$.
- **the etching depth:** No significant relation between the etching depth and the quality factor can be extrapolated from the gathered data. Indeed, Q increases within the etching depth for the standard parametric study but the inverse relation is observed in our extended study.
- **the IDT's coverage:** The standard studies shows a peak in the quality factor when $coverage = 50$ [%].

- **the thickness of the piezoelectric layer:** As for the etching depth, a different behavior is observed between the standard studies (where Q decreases with t_{piezo}) and the extended study (where we observe a significant increase of Q within t_{piezo}).
- **the thickness of the metallic layer:** While a maximum seems to be reached for $t_{Pt} = 75$ $[nm]$ in the standard studies, Q decrease almost linearly within t_{Pt} in the extended study.

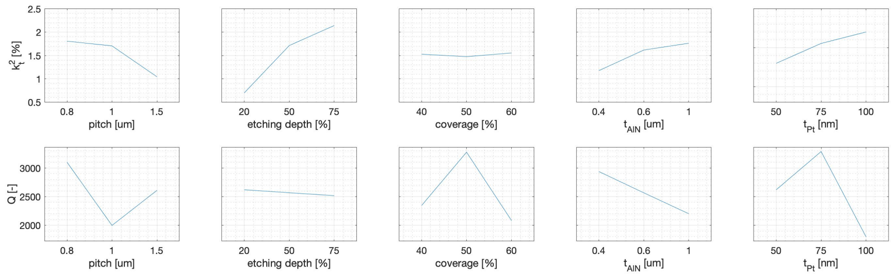

Figure 3.13: Main effect of AlSc(0.17)N SAW/BAW hybrid resonator's geometry onto its electro-mechanical coupling (k_t^2) and quality factor (Q). Simulation parameters : Substrate=SiC

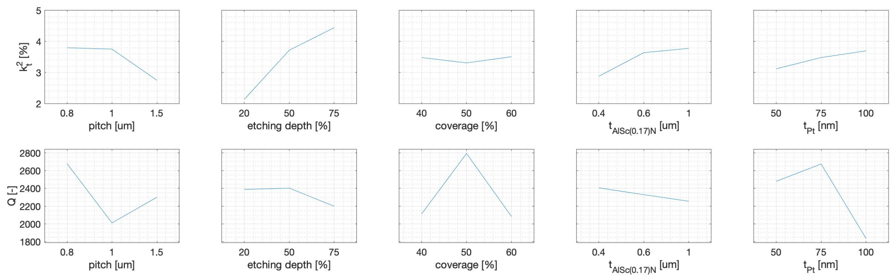

Figure 3.14: Main effect of AlSc(0.17)N SAW/BAW hybrid resonator's geometry onto its electro-mechanical coupling (k_t^2) and quality factor (Q). Simulation parameters : Substrate=SiC

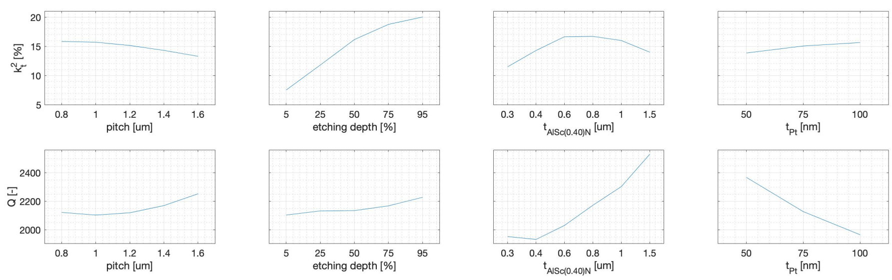

Figure 3.15: Main effect of AlSc(0.4)N SAW/BAW hybrid resonator's geometry onto its electro-mechanical coupling (k_t^2) and quality factor (Q). Simulation parameters : $coverage = 50$ [%]; Substrate=SiC

Note on the validity of the above conclusions: First of all, we wanted to point out the statistical nature of the conducted study. Any of the points represented in the figures 3.13, 3.14 and 3.15, represents a manufacturable geometry. There are the result of a statistical study of all the designs point with a given parameter value. Therefore, as mentioned earlier, the trends may be biased because of the finite nature of our design set.

Moreover, we are trying to find a relation between the geometry and the performance of devices based on three different piezoelectric materials. As explained in the previous section, the relative physical properties between the piezoelectric and substrate materials may be as important as their absolute values. Therefore, some the differences between studies may be explained by this change of piezoelectric material. For example, it may be possible that the decrease of the acoustic wave velocity due to the high doping value of AlSc(0.40)N leads to the apparition of a new dominant mechanism at the interface piezo-substrate which may explain the difference in quality factor behavior.

We also wanted to remind the reader that the 2D infinite approximation of the unity cell simulation leads to an over-estimation of the quality factor. However, we make the assumption that the relative values are representative of the behavior of the real device.

3.3.3 Interaction Plot

An interaction plot is a secondary order statistical tool which allow to study the interaction of parameters with performances. One graph is generated for each parameter. It represents, by a line plot, the mean value of the performance (k_t^2 and Q in our case) in function of the aforementioned parameter.
In the figure 3.16, we presents the interaction plot for the coupling and quality factors for SAW/BAW hybrid devices based on AlSc(0.40)N.

The existence of higher order relations questions the quality of the main effect plots presented before. Indeed, since the design set is finite, the main effect plots' results may be biased. In particular, analyzing the figure 3.15 shows that k_t^2 is inversely proportional to the pitch (we observe a difference of 2.5% between $pitch = 0.8$ $[\mu m]$ and $pitch = 1.6$ $[\mu m]$). However, with the same data set, we see in 3.16, that a maximum of $k_t^2 = 17.2 \pm 0.5$ [%] can be achieved regardless of the pitch's value.

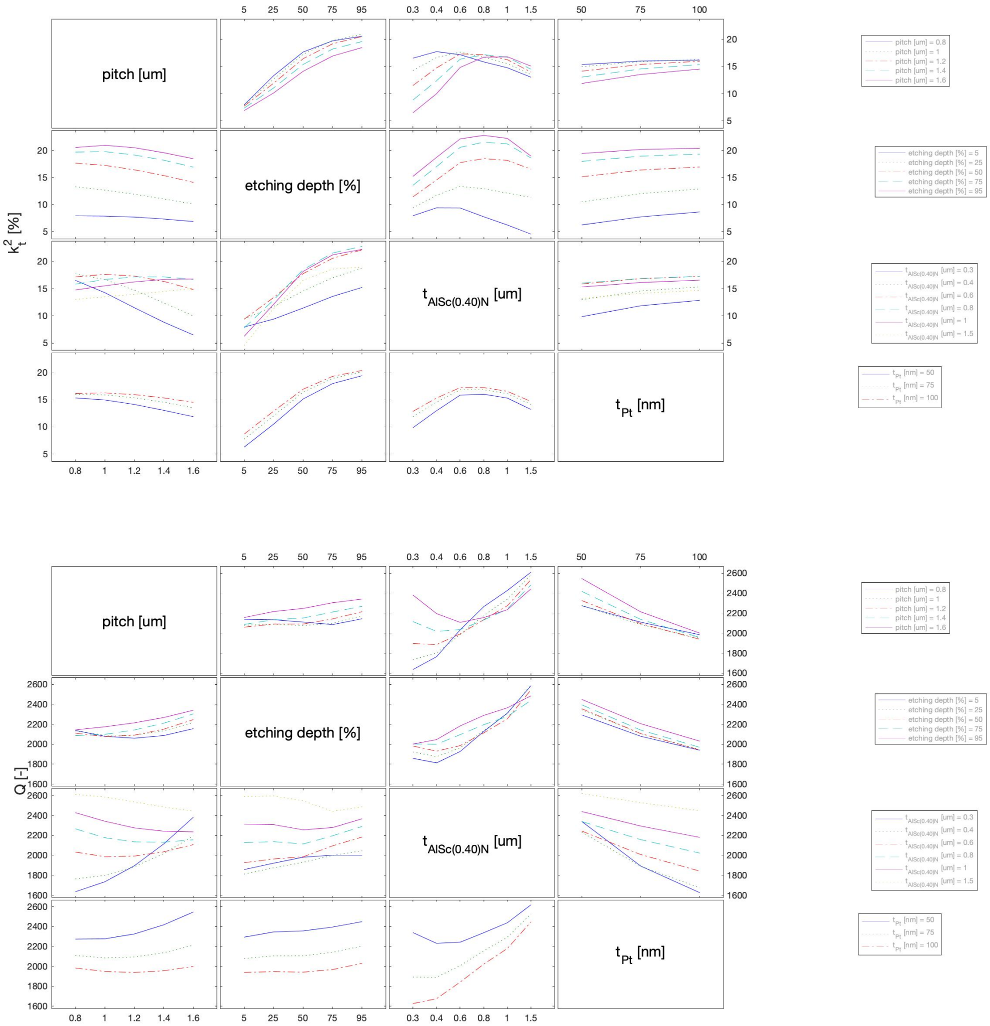

Figure 3.16: Extended parametric study of AlSc(0.4)N SAW/BAW hybrid resonator's geometry onto its electro-mechanical coupling (k_t^2) and quality factor (Q). Simulation parameters : $coverage = 50$ [%]; Substrate=SiC

3.3.4 SAW/BAW hybrid resonator

Knowing the acoustic wave's velocity in the piezoelectric layer, a good approximation[9] of the resonance frequency can be found for both SAW and BAW resonators:

$$SAW \; : \qquad f_{res} = \frac{c_{acoustic}}{pitch} \tag{3.7}$$

$$BAW \; : \qquad f_{res} = \frac{c_{acoustic}}{2 * t_{piezo}} \tag{3.8}$$

In the figure 3.17, the resonance frequency decreases almost linearly with both the pitch and the thickness of the piezoelectric layer. This result demonstrates the hybrid behavior of our device. A fitted formula may be determined by looking into compositions of equations 3.7 and 3.8.

In the introduction of their 2017 paper [30], Paschenko and al. describe the SAW/BAW hybrid resonators as an array of BAW sensors that excites a SAW in the non-piezoelectric substrate. Even if this statement is correct when the piezoelectric layer is totally etched, our interaction plot shows mixed SAW/BAW mode for intermediate etching ratio. Indeed, the figure 3.18 shows that even if 95% of the piezoelectric layer is etched, the resonance lower with the pitch (from 1.346 $[GHz]$ when $pitch = 0.8$ $[\mu m]$ to 1.224 $[GHz]$ when $pitch = 1.6$ $[\mu m]$).

Since this behavior may also be explained by a complex interaction of the piezo-metal-substrate stack, a further investigation shall be conducted to characterize this hybrid acoustic mode.

[9] If we do not consider the interactions with the substrate.

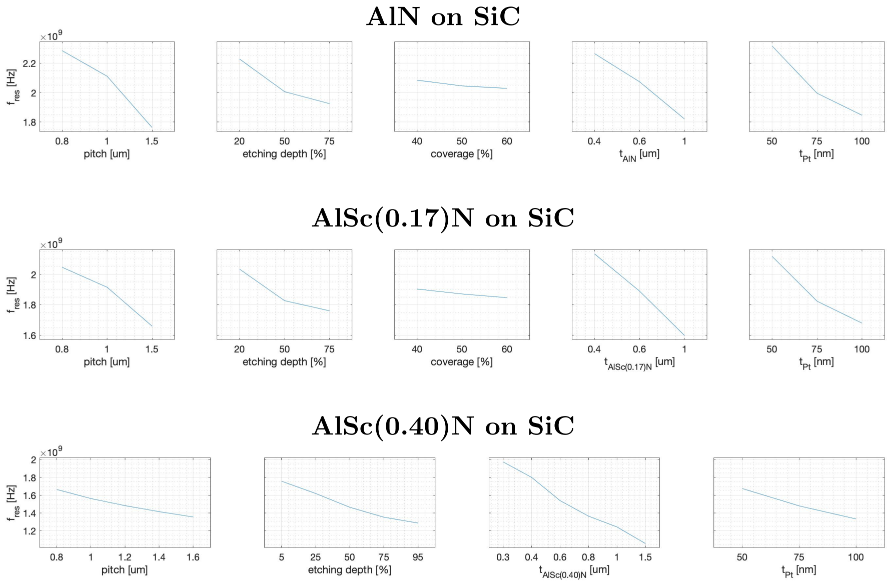

Figure 3.17: Main effect of design parameters on first mode's resonance frequency (f_{res}) of AlN, AlSc(0.17)N and AlSc(0.40)N based SAW/BAW hybrid resonators. Simulation parameters : $coverage = 50$ [%]; Substrate=SiC

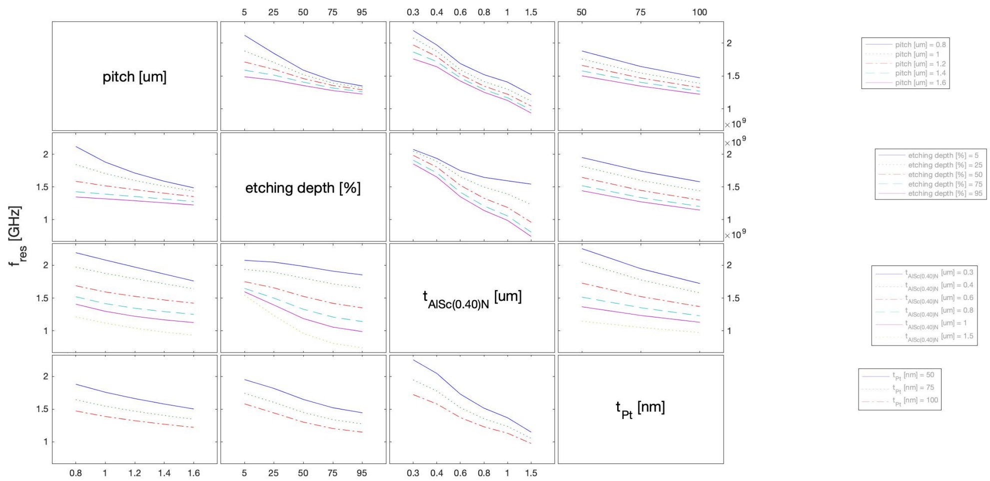

Figure 3.18: Interaction plot of the extended parametric study of AlSc(0.4)N SAW/BAW hybrid resonator's geometry onto its first mode's resonance frequency (f_{res}). Simulation parameters : $coverage = 50$ [%]; Substrate=SiC

3.3.5 Optimal Thickness-Over-Pitch Ratio

In their 2016 paper, Paschenko and al. [29] identify an optimal thickness-over-pitch ratio which maximize the amplitude of SAW excited in an SAW/BAW hybrid resonator. At first sight, the figure 3.3.3 seems to confirm the value of $r_{opt} = \frac{t_{piezo}}{pitch} = 0.5$ $[-]$.
However, we noticed that any of the designs that maximize k_t^2 in our parametric study respects this ratio.
In the figure 3.19, we present the relation between k_t^2 and r_{opt}. We separate the designs according to their *etching depth* value. Then we approximate the raw data with 6th order polynomials (plain lines) and identify the maximum of these curves (filled triangles). We notice that the optimal thickness-over-pitch ratio shift with the value of etching depth. For small etching values, our result ($r_{opt} = 0.41$ $[-]$) matches the similar study conducted by Hao and al. [1] on SAW devices[10]. However, this optimal value increases to $r_{opt} = 0.7 \pm 0.05$ $[-]$ for higher etching depth (*etching depth* > 50 $[\%]$).

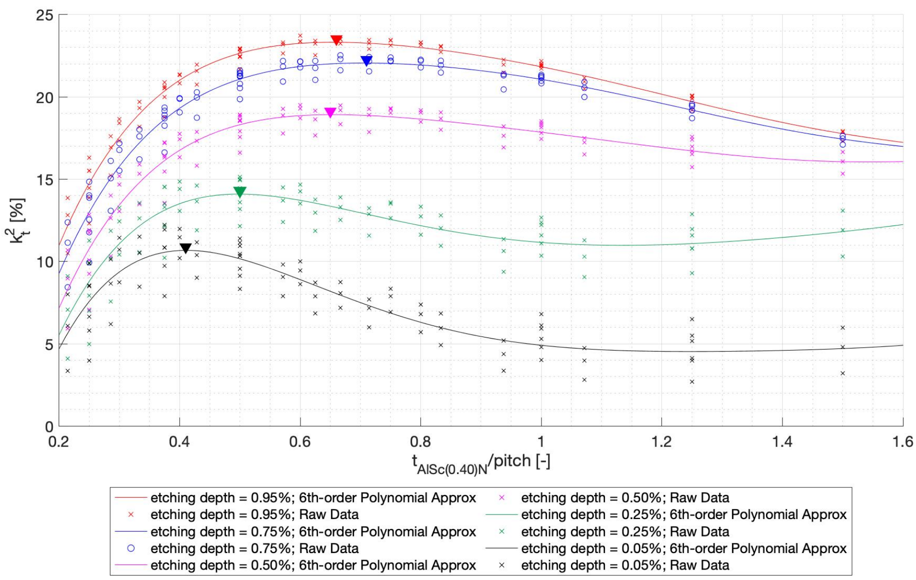

Figure 3.19: Evolution of the optimal thickness-over-pitch ratio for AlSc(0.40)N SAW/BAW hybrid resonators in function of the etching depth. Results of an extended parametric simulation. each cross represent a different design. *coverage* $= 50$ $[\%]$ and the substrate material (SiC) are constant all along the study. The other parameters have been sweep. The filled triangles represent the peaks of the approximation curves.

[10] They found a maximum when $\frac{t_{piezo}}{pitch} \in [0.3; 0.5]$ $[-]$.

Chapter 4

Simulation - Finite Device

4.1 Simulation Setup

The set up of our finite device is a direct adaptation of the unity cell simulation. From left to right, the configuration of the FD is as follow : a PML - a domain to study the propagation of the wave up to $3 \cdot \lambda_{SAW}$ on the left - an array of 10 UC used as left reflector - an array of 50 UC (main resonator) - an array of 10 UC used as right reflector - a domain to study the propagation of the wave up to $3 \cdot \lambda_{SAW}$ on the right - a PML.

Since all the unity cells were a copy of the initial simulation, all conditions described in the previous chapter are automatically applied (except the periodicity condition which is removed). We then apply the conditions related to the material (boundary + domains) to the newly created geometry.

We finally remove the reflector's UC from the terminals (electrostatic condition). Their new attribution will be explained later on since it is the subject of our study on the wave's confinement.

NOTE: For obvious manufacturing reasons, the piezoelectric is etched everywhere but bellow the IDT (see fig. 4.1).

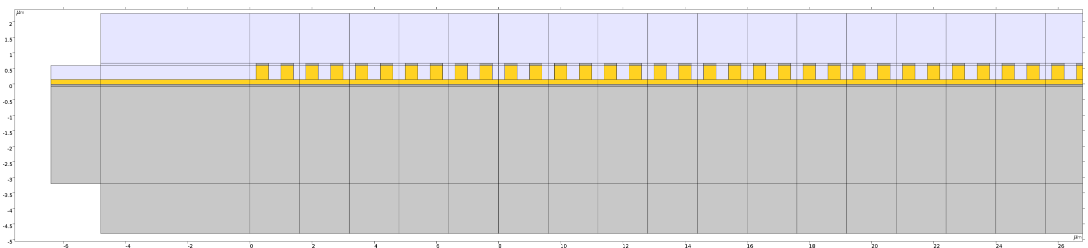

Figure 4.1: Geometry of the right end of the FD simulation. Figure parameters : $pitch = 0.8$ [μm]; $etching\ depth = 75$ [%]; $t_{AlN} = 0.6$ [μm]; $t_{Pt} = 75$ [nm]; $coverage = 50$ [%] / The material are as follow : light blue = air; dark grey = Platinum ; yellow = piezoelectric material ; light grey = substrate (SiC)

4.2 Wave Confinement

As mentioned before, the quality factor computed in the UC simulation may be overestimated because loss mechanisms are ignored with the infinite 2D approximation. A new loss mechanism is introduced with the FD simulation. Indeed, energy can be lost in the PML with the transverse horizontal propagation of the acoustic wave. Since we want to design a finite device which operate in a 1-port/standing wave operation, it is primordial to ensure the confinement of the wave in the IDT region.
In this section, we will investigate reflectors' design to trap the acoustic wave in our region of interest.

4.2.1 Baseline

We measure the efficiency of our acoustic wave trapping by comparing the displacement of our structures at different level of the piezoelectric layer (see fig. 4.2). The first cut-line is defined at 99% of the layer while the second is set at 49.5% (which corresponds to 99% of the unetched material). We consider the ratio between the maximum displacement (at the center of the IDT) and the displacement far from the structure (last peak before the PMLs) as a good indicator of the trapping efficiency.
The material losses, due to the propagation of vertical longitudinal acoustic waves in the substrate, is orders of magnitude higher than the one of interest. Therefore, we decided to deactivate all material losses for this study. Because of this alteration, the absolute value of the quality factor explodes. However, we assume that the relative value of Q between the different configurations reflects the behavior of the studied loss mechanism.
To ensure meshing and structural coherency between the configurations, we decided to keep the geometry as described earlier. Therefore, we reduced the UC array's size from 70 (50 for IDT + 2x10 for the reflectors) to 50.
The baseline's values are recorded in the table 4.1.

	Variable	Units	Value
	Quality Factor	$[-]$	$3.48E+07$
99 %	Maximum displacement	$[nm]$	≈ 8.5
	Far-field displacement	$[nm]$	NA
	Ratio	[%]	NA
49.5 %	Maximum displacement	$[nm]$	≈ 5
	Far-field displacement	$[nm]$	$\approx 2E-01$
	Ratio	[%]	4.0
	$\frac{Max(99\%)}{Far-field(49.5\%)}$	[%]	2.4

Table 4.1: Q-factor, maximum and far-field displacement values at resonance frequency from the FD simulation of a SAW/BAW hybrid resonator without the presence of reflectors. Simulation's parameters : $pitch = 0.8$ $[\mu m]$; $etching\ depth = 50[\%]$; $coverage = 50$ $[\%]$; $t_{AlN} = 0.4$ $[\mu m]$; $t_{Pt} = 50$ $[nm]$; Substrate=SiC - Data extracted from figure 4.2

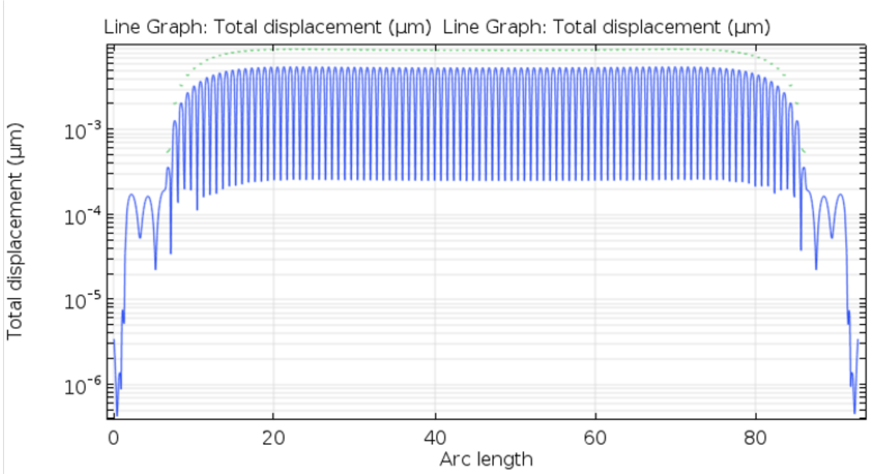

Figure 4.2: Displacement at resonance frequency along horizontal cut-lines (99% and 10% of the AlSc(0.40)N layer) from the FD simulation of a SAW/BAW hybrid resonator without the presence of reflectors. Simulation's parameters : $pitch = 0.8$ [μm]; $etching\ depth = 50$[%]; $coverage = 50$ [%]; $t_{AlN} = 0.4$ [μm]; $t_{Pt} = 50$ [nm]; Substrate=SiC - The green line corresponds to the 99% cut-line. The blue line corresponds to the 49.5% cut-line. The displacement is not defined where the piezoelectric layer is etched: this explains the dashed look of the 99% cut-line.

4.2.2 Reflector with 1-lambda-periodicity

In this configuration, we want to determine the impact of a series of $1\lambda_{SAW}$-periodicity floating IDT on the confinement of the acoustic wave.

The resonators are composed of 5 pairs of fingers with a periodicity of $1 \cdot pitch$. One reflector is placed at each side of the resonator, separated by $1 \cdot pitch$ from the last finger of device's IDT. We create 2 floating potentials and apply them to the contour of the resonators electrodes. we alternate the potentials in a way that consecutive fingers are not connected together. We duplicate these electrostatics's conditions for the second reflector[1].

The simulation of this configuration shows a deterioration of the quality factor from $3.48E+07$ (baseline) to $2.25E+07$. However, the trapping is improved since the ratio between the maximum and far-field displacements decreases from 2.5% (baseline) to 0.61%.

As described in the section 2.2.1, the quality factor is a metric which describes the coupling between our resonator and its environment. Thus, these, a priory, opposite responses can be explained by an unexpected coupling behavior between the resonator and the reflectors. Indeed, the figure 4.3 demonstrates an excessive excitation of the reflectors. The displacement in the reflectors reaches $1E-01$ [nm] which is the same order of magnitude than the baseline's far-field value.

Even if the $1\lambda_{SAW}$ periodicity is not in favor of the quality factor, the high displacement in the reflector demonstrate the capability of our design to operate in a 2-ports configuration.

[1]The two reflectors are not connected, two new floating potential are created.

	Variable	Units	Value
	Quality Factor	$[-]$	$2.25E+07$
99 %	Maximum displacement	$[nm]$	≈ 9
	Far-field displacement	$[nm]$	NA
	Ratio	$[\%]$	NA
49.5 %	Maximum displacement	$[nm]$	≈ 6
	Far-field displacement	$[nm]$	$\approx 5.5E-02$
	Ratio	$[\%]$	0.92
	$\frac{Max(99\%)}{Far-field(49.5\%)}$	$[\%]$	0.61

Table 4.2: Q-factor, maximum and far-field displacement values at resonance frequency from the FD simulation of a SAW/BAW hybrid resonator in the presence of reflectors with a $1\lambda_{SAW}$-periodicity. Simulation's parameters : $pitch = 0.8$ $[\mu m]$; $etching\ depth = 50[\%]$; $coverage = 50$ $[\%]$; $t_{AlN} = 0.4$ $[\mu m]$; $t_{Pt} = 50$ $[nm]$; Substrate=SiC - The resonators are composed of 5 pairs of fingers with a periodicity of $1 \cdot pitch$. These fingers are alternatively allocated to one floating potential, forming thus a "reflective" IDT with a $1\lambda_{SAW}$-periodicity. One reflector is placed at each side of the resonator, separated by $1 \cdot pitch$ from the last finger of device's IDT. - Data extracted from figure 4.3

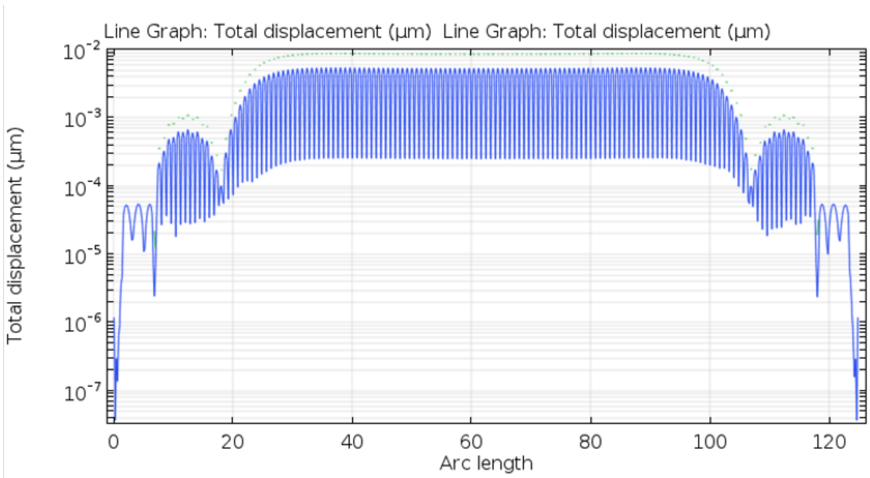

Figure 4.3: Displacement at resonance frequency along horizontal cut-lines (99% and 10% of the AlSc(0.40)N layer) from the FD simulation of a SAW/BAW hybrid resonator in the presence of reflectors with a λ_{SAW}-periodicity. Simulation's parameters : $pitch = 0.8$ $[\mu m]$; $etching\ depth = 50[\%]$; $coverage = 50$ $[\%]$; $t_{AlN} = 0.4$ $[\mu m]$; $t_{Pt} = 50$ $[nm]$; Substrate=SiC. - The resonators are composed of 5 pairs of fingers with a periodicity of $1 \cdot pitch$. These fingers are alternatively allocated to one floating potential, forming thus a "reflective" IDT with a λ_{SAW}-periodicity. One reflector is placed at each side of the resonator, separated by $1 \cdot pitch$ from the last finger of device's IDT. - The green line corresponds to the 99% cut-line. The blue line corresponds to the 49.5% cut-line. The displacement is not defined where the piezoelectric layer is etched: this explains the dashed look of the 99% cut-line.

4.2.3 Reflector with 2-lambda-periodicity

In this configuration, we short the 10 reflectors' fingers through a unique floating potential (one for each reflector). It forms thus a resonator with a $2\lambda_{SAW}$-periodicity.
Shorting two consecutive fingers impose the same potential in the piezoelectric layer beneath them. Therefore, for a standing wave to exist, the only possibility (solution to the wave equation) is no displacement under the reflectors.
As shown in the figure 4.4, the theory is confirmed: the displacement decreases exponentially bellow the resonator. Within a $2\lambda_{SAW}$ configuration, the reflectors confined the energy into the resonator: the ratio between the maximum and far-field displacements decreases from 2.5% (baseline) to 0.17%. This interpretation is confirmed by a 28% increase of the quality factor: from $3.48E+07$ $[-]$ (baseline) to $4.45E+07$ $[-]$

	Variable	Units	Value
	Quality Factor	$[-]$	$4.45E+07$
99 %	Maximum displacement	$[nm]$	≈ 9
	Far-field displacement	$[nm]$	NA
	Ratio	$[\%]$	NA
49.5 %	Maximum displacement	$[nm]$	≈ 5.5
	Far-field displacement	$[nm]$	$\approx 1.5E-02$
	Ratio	$[\%]$	0.27
	$\frac{Max(99\%)}{Far-field(49.5\%)}$	$[\%]$	0.17

Table 4.3: Q-factor, maximum and far-field displacement values at resonance frequency from the FD simulation of a SAW/BAW hybrid resonator in the presence of reflectors with a $2\lambda_{SAW}$-periodicity. Simulation's parameters : $pitch = 0.8$ $[\mu m]$; $etching\ depth = 50[\%]$; $coverage = 50$ $[\%]$; $t_{AlN} = 0.4$ $[\mu m]$; $t_{Pt} = 50$ $[nm]$; Substrate=SiC - The resonators are composed of 10 shorted fingers with a periodicity of $1 \cdot pitch$. One reflector is placed at each side of the resonator, separated by $1 \cdot pitch$ from the last finger of device's IDT. - Data extracted from figure 4.4

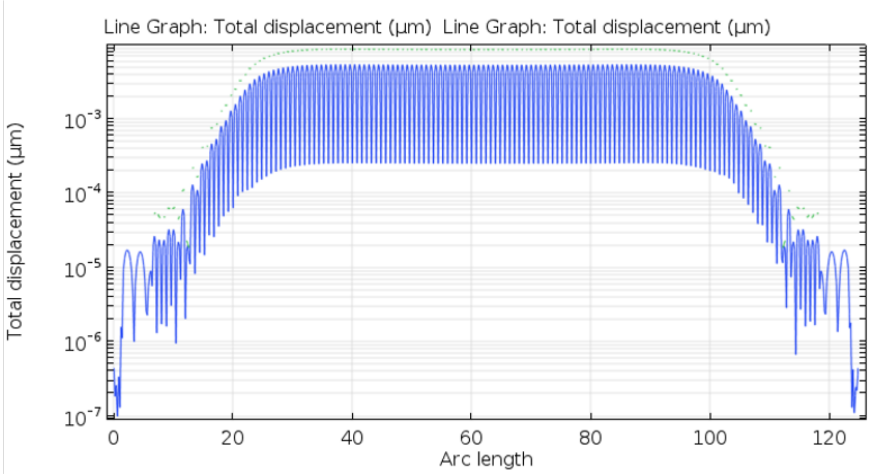

Figure 4.4: Displacement at resonance frequency along horizontal cut-lines (99% and 10% of the AlSc(0.40)N layer) from the FD simulation of a SAW/BAW hybrid resonator in the presence of reflectors with a $2\lambda_{SAW}$-periodicity. Simulation's parameters : $pitch = 0.8$ [μm]; $etching\ depth = 50$[%]; $coverage = 50$ [%]; $t_{AlN} = 0.4$ [μm]; $t_{Pt} = 50$ [nm]; Substrate=SiC - The resonators are composed of 10 shorted fingers with a periodicity of $1 \cdot pitch$. One reflector is placed at each side of the resonator, separated by $1 \cdot pitch$ from the last finger of device's IDT. - The green line correspond at the 99% cut-line. The blue line correspond at the 49.5% cut-line. The displacement is not defined where the piezoelectric layer is etched: this explained the dashed look of the 99% cut-line.

4.3 Design Performances

The secondary objective of our parametric study (see section 3.3) is to find a combination of parameters which maximize the device's performances.
Three different metrics can be used to measure the performance of the system: $F_{cost} = k_t^2$, $F_{cost} = Q$ or $F_{cost} = k_t^2 \cdot Q$. Moreover, because the bandwidth allocation in the aerospace industry is quite restrictive, the resonance frequency cannot be ignored.
In that study, we assumed the relative value of the quality factor is representative of the behavior of the real device. However, its absolute value may differ because of the 2D-infinite approximation. Moreover, multiple bands are available for sensing and the extended study has shown that the frequency can easily be tuned. For all these reasons, our final choice fell on $F_{cost} = k_t^2$
Running the finite simulation allows us to validate our previous results and to have a better approximation of the absolute value of the quality factor.

		Simulation Setup						Performances				
		$pitch$ $[\mu m]$	$etching\ depth$ [%]	$coverage$ [%]	t_{piezo} $[\mu m]$	t_{Pt} $[nm]$	Substrate	f_{res} $[GHz]$	f_{anti} $[GHz]$	k_t^2 [%]	Q [−]	$Q \cdot k_t^2$ [−]
UC	AlN	0.8	75	60	0.6	75	SiC	2.082	2.106	2.81	1785	50
UC	AlSc(0.17)N	0.8	75	50	0.6	50	SiC	1.832	1.875	5.53	1850	102
UC	AlSc(0.40)N (A)	1.0	95	50	0.6	75	SiC	1.358	1.522	23.72	2130	505
UC	AlSc(0.40)N (B)	0.8	75	50	0.3	50	SiC	2.417	2.638	18.91	1805	341
FD	AlN	0.8	75	50	0.6	75	SiC	2.082	2.105	2.67	1785	48
FD	AlSc(0.17)N	0.8	75	50	0.6	50	SiC	1.851	1.895	5.60	1870	105
FD	AlSc(0.40)N (A)	1.0	95	50	0.6	75	SiC	1.359	1.521	23.48	2105	494
FD	AlSc(0.40)N (B)	0.8	75	50	0.3	50	SiC	2.418	2.635	18.65	1950	365

Table 4.4: Optimized designs and performances of AlN, AlSc(0.17)N and AlSc(0.40)N hybrid SAW/BAW resonators for both UC and FD simulations - The design points AlN, AlSc(0.17)N and AlSc(0.40)N (A) are the sets of parameters which achieved the highest electromechanical coupling factor during our parametric study. AlSc(0.40)N (B) is the best set with a resonance frequency in the $2.35 - 2.45$ $[GHz]$ range. The FD simulation do not allow a *coverage* different than 50%. Which explain the difference between the AlN's UC and FD simulations.

For each piezoelectric material, we present in the table 4.4 the optimal parameters set as well as their performances (both UC and FD simulations). The performances between the UC and FD simulations are quite similar: we record a 1.5% and 5% variations of k_t^2 and Q respectively.
The comparison of the FoM of our SAW/BAW hybrid resonators with the experimental results of the literature is quite astonishing (see fig. 4.5). Indeed, we achieve simultaneously high quality factors ($Q_{AlSc(0.40)N} \approx 1800$; $Q_{AlSc(0.17)N} \approx 1900$; $Q_{AlSc(0.40)N} \approx 2100$) and high electromechanical coupling factors ($k^2_{t,AlN} = 2.67$ [%]; $k^2_{t,AlSc(0.17)N} = 5.60$ [%]; $k^2_{t,AlSc(0.40)N} = 23.48$ [%]). Our SAW/BAW hybrid resonator based on AlSc(0.40)N thin film reaches the highest Figure of Merit ever recorded for an AlN/AlScN based acoustic resonators: $k_t^2 \cdot Q = 494$ $[-]$.

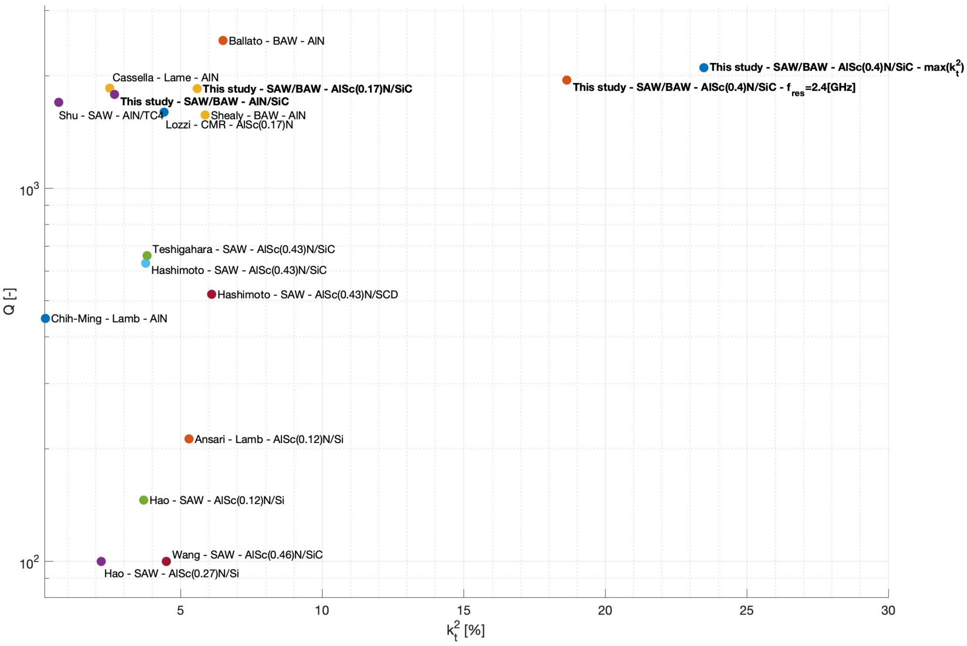

Figure 4.5: Comparison of performances between optimized design and literature in term of electro-mechanical coupling (k_t^2) and quality factor (Q) - Literature's experimental values from [1], [5], [11], [21], [24], [25], [26], [28], [31], [32], [33], [34]. The results from this study were simulated using our FD setup. Optimized parameters for AlN: *pitch* $= 0.8$ $[\mu m]$; *etching depth* $= 75[\%]$; *coverage* $= 60$ $[\%]$; $t_{AlN} = 0.6$ $[\mu m]$; $t_{Pt} = 50$ $[nm]$; Substrate=SiC / Optimized parameters for AlSc(0.17)N: *pitch* $= 0.8$ $[\mu m]$; *etching depth* $= 75[\%]$; *coverage* $= 50$ $[\%]$; $t_{AlN} = 0.6$ $[\mu m]$; $t_{Pt} = 50$ $[nm]$; Substrate=SiC / Optimized parameters for AlSc(0.40)N: *pitch* $= 1.0$ $[\mu m]$; *etching depth* $= 95[\%]$; *coverage* $= 50$ $[\%]$; $t_{AlN} = 0.6$ $[\mu m]$; $t_{Pt} = 75$ $[nm]$; Substrate=SiC / AlSc(0.40)N at 2.4 $[GHz]$: *pitch* $= 1.0$ $[\mu m]$; *etching depth* $= 95[\%]$; *coverage* $= 50$ $[\%]$; $t_{AlN} = 0.6$ $[\mu m]$; $t_{Pt} = 75$ $[nm]$; Substrate=SiC

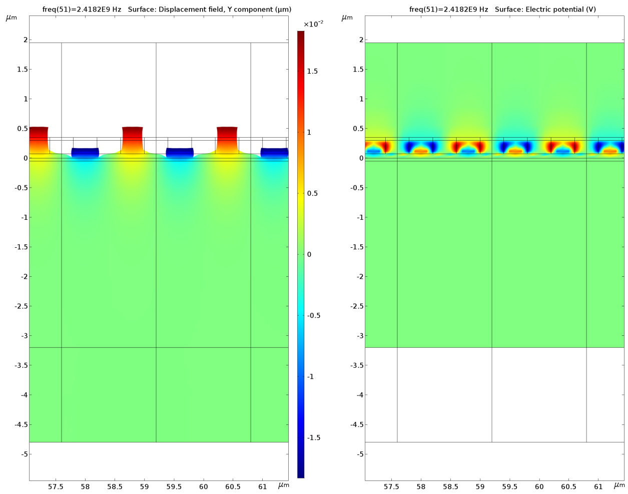

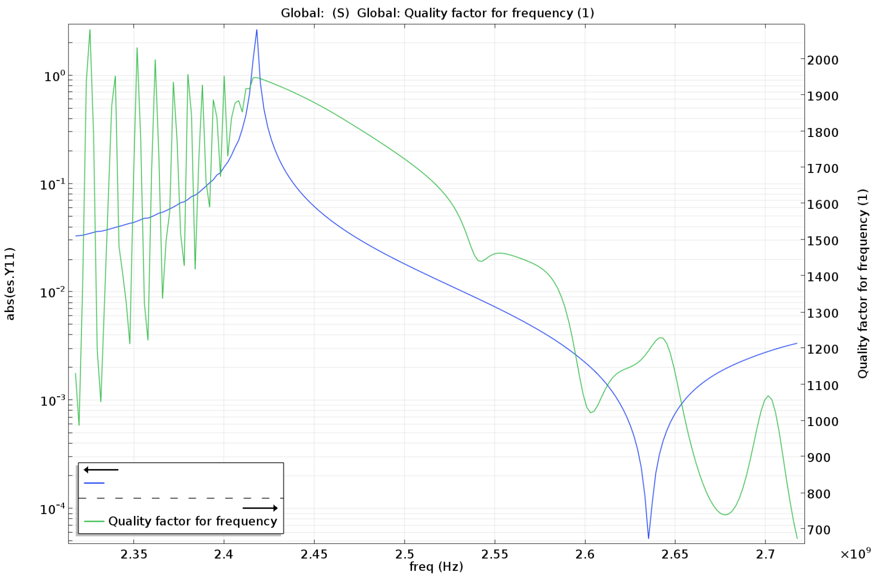

Figure 4.6: Representation of the vertical displacement, electric potential, terminal's impedance and quality factor of an AlSc(0.40)N hybrid resonator from the FD simulation. Simulation parameters : $pitch = 1.0\ [\mu m]$; $etching\ depth = 95[\%]$; $coverage = 50\ [\%]$; $t_{AlN} = 0.6\ [\mu m]$; $t_{Pt} = 75\ [nm]$; Substrate=SiC

Chapter 5

Manufacturing

5.1 Process Flow

Step	Description	Cross-section after process
01	**Substrate: HR Si** **Photolitho for lift-off** Machine: EVG150/MLA150 Resist: AZ1512 Thick: 1.1 um 0.48 LOR Mask #1	
02	**Bottom Electrode sputtering** Machine:Pfeiffer Spider 600 Materials: Ti/Pt Thickness: 10nm/50nm	
03	**Lift-off** Machine: Develop bench Remover 1165	
04	**Piezo layer & top Electrode**] **& Hard Mask sputtering** Machine: Pfeiffer Spider 600 Materials : AlScN/Pt/SiO2 Thickness : 400/50/500nm	
05	**Openings Photolitho Resist** Machine: EVG150/MLA150 Resist: AZ1512 Thick: 1.1 um 0.48 LOR Mask #2	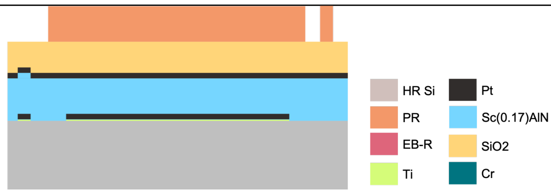

06	**Hard mask & top metal Dry Etch** Material : SiO2 / Pt Machine: SPTS Depth : 500 nm	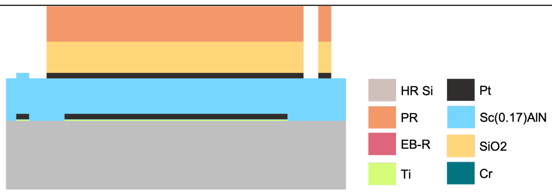
07	**Resist strip** Machine: Develop bench Remover: 1165	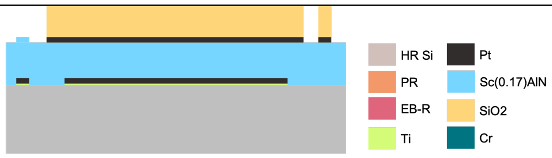
08	**Protective Layer Coating** Resist: AZ1512 Thick: 1.1 um 0.48 LOR	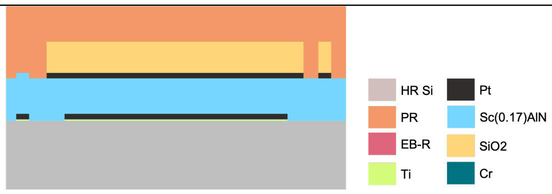
Dicing (chip size : 17x17mm2) – Machine: Disco DAD321		
09	**Protective Layer strip** Chip level Machine: Develop bench Remover 1165	
10	**Ebeam-Resist Coating** Chip level Machine: ATMsse OPTIspin SB20 – EBPG5000 EB-R : CSAR 62 – 600 nm	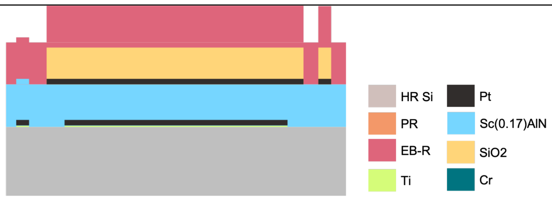
11	**Conductive Layer sputtering** Machine:LAB600 or EVA760 Materials: Cr Thickness: 30nm	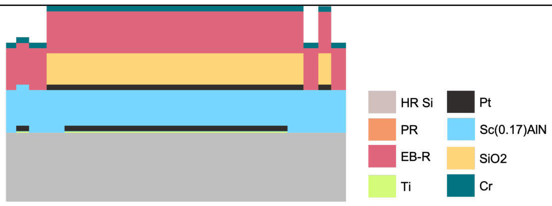
12	**Openings Ebeam-Resist** Chip level Machine: Vistec EPBG5000ES - Ebeam Mask #3: IDT + top pads	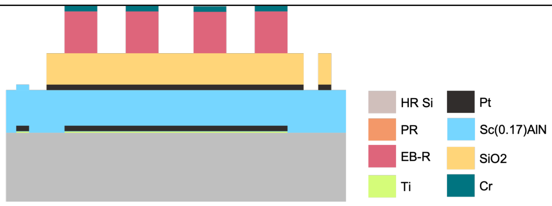

13	**Hard mask Dry Etch** Chip level Material : SiO2 Machine: SPTS Depth : 500 nm	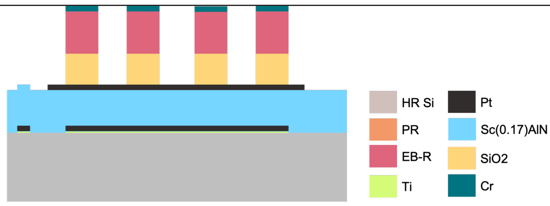
14	**Piezo Dry Etch** Chip level Material : Pt/AlScN Machine: STS Depth : 50/300 nm	
15	**Hard mask strip** Chip level Machine: HF Bath / μetch	

Table 5.1: Process flow approved by EPFL's Center of MicroNanotechnology(CMi)

5.2 Mask Layout Design

5.2.1 Layer description

The Mask Layout is composed of 4 layers:

- **Layer 01:** The first layer (Mask #1) is used during the lift-off of the bottom electrode. A study of Lozzi and al. [6] demonstrated that the best growing seed for epitaxial AlScN is AlN. However, it complexifies the process flow. Instead, we use the work of Dubois and al. [35] which shows that growing AlN layer onto Pt enhance its d_{33} piezoelectric coefficient. Therefore, we maximize the ratio of metalization of the bottom electrode (see fig.5.2): we only remove a small square around the bottom electrode and bellow the pads to limit the parasitic capacitance.

- **Layer 02:** The second layer (Mask #2) is used to prepare the ebeam lithography. To save time during the ebeam lithography, we remove the top metal far from the devices where the resolution is not critical. Moreover, we use this step to create markers with high contrast to be used during the alignment of ebeam mask.

- **Layer 03:** The third layer (Mask #3-1) is used during the ebeam lithography. It is used to write the CSAR where the nanometric resolution is not required (i.e. for the pads and the intersection with the second layer). During this writing, we will use a $100nm$ pixel and beam size.

- **Layer 04:** The final layer (Mask #3-2) is used during the ebeam lithography. It is used to write the CSAR with an higher precision than layer 3 (i.e. mainly for the IDTs and reflectors). During this writing, we will use a $50nm$ pixel and beam size (we may consider smaller pixel size if $pitch < 0.8$ $[\mu m]$).

To draw the layers that we present in this chapter, we used a mix of scripting (mainly at device's array level) and manual operations.

NOTE: The diverse alignment marks and test structures are exported from CMi's template then adapted to our process flow (inverted/scaled).

5.2.2 Layout description

The first step of the mask design is to choose the shape of the chips and organise their disposition to fit as many as possible in a 4-inches wafer. We choose 17mm-square chips because it is a good compromise between the number of chips and their handleability. As shown in figure 5.1, we fit a total of 16 chips onto the wafer. We identify the chips according to their position onto the wafer using the same system as chessboards[1,2].
The second step was to create a symbol to draw the devices (see fig. 5.2. This step is done using C++ scripting in CleWin. We parametrize the geometry using the parameters presented in the previous chapter and the geometry of the measurement probe. Furthermore, we create an array of the same design with a different number of fingers with and without reflectors.
In order to measure the properties of the devices such as parasitic resistivity and capacitance, we create a total of three devices per design. The first one has no fingers (for capacitance measurements), the second has extended (shorted) fingers (for resistivity measurement) and the third one is the operational device.
Once the device arrays are designed, it is time to create the chips' symbol (see fig. 5.3). We place 6 device arrays (with different geometries) on each chips.
Then, we place the alignment, dicing marks and the test structures.
Finally, it is time to lay the chips onto the wafer (see fig. 5.1), add global identifiers and symbols.

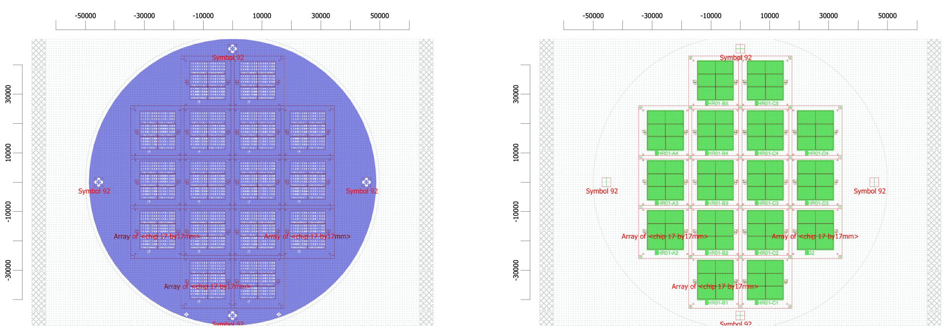

(a) (b)

Figure 5.1: Masks for the manufacturing of SAW/BAW hybrid resonators - wafer level. Generated with CleWin 5 (axis unit: [μm]). (a) Layer 01 : Mask #1 - lift-off bottom electrode. (b) Layer 2: Mask #2 - Definition of alignment marks for e-beam.

[1]columns are identified with a letter (A to D) and the rows with numbers (1 to 5). The origin is at the bottom left.
[2]The identifiers A1, D1, A5 and D5 are not attributed

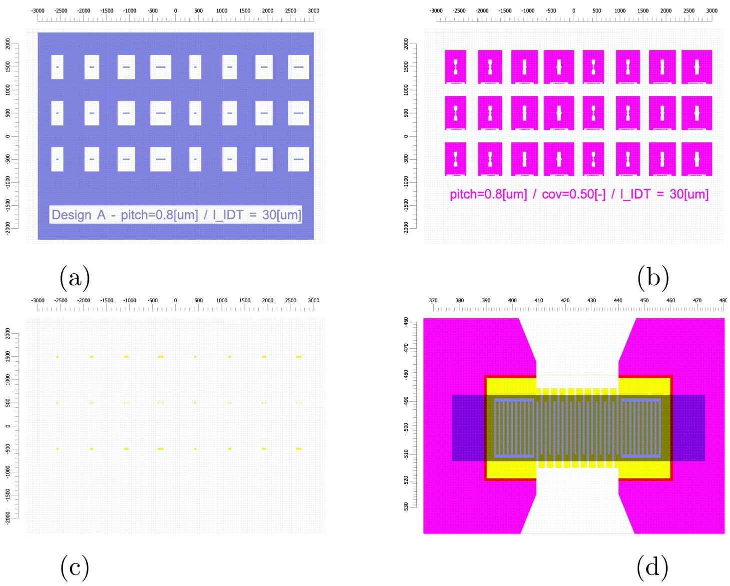

Figure 5.2: Masks for the manufacturing of SAW/BAW hybrid resonators - device level. Generated with CleWin 5 (axis unit: $[\mu m]$). (a) Layer 01 : Mask #1 - lift-off bottom electrode. (b) Layer 3: Mask #3-1 - Mask with large pixel size for ebeam lithography of probe pads. (c) Layer 4: Mask #3-2 - Mask with small pixel size for ebeam lithography of IDTs. (d) Layer 1,3,4: Zoom on a resonator.

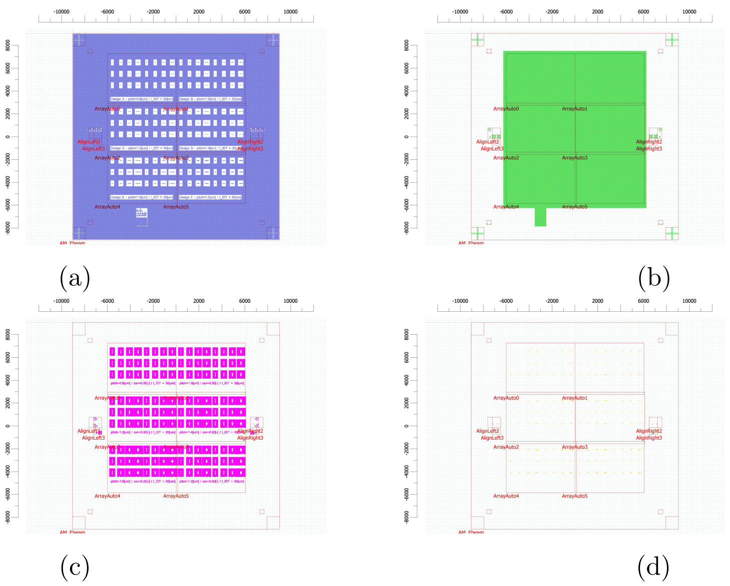

Figure 5.3: Masks for the manufacturing of SAW/BAW hybrid resonators - chip level. Generated with CleWin 5 (axis unit: $[\mu m]$). (a) Layer 01 : Mask #1 - lift-off bottom electrode. (b) Layer 2: Mask #2 - Definition of alignment marks for e-beam. (c) Layer 3: Mask #3-1 - Mask with large pixel size for e-beam of probe pads. (d) Layer 4: Mask #3-2 - Mask with small pixel size for e-beam of IDTs.

5.3 HR01 - Test wafer

The final step of this work is the manufactufacturing a series of devices to validate our simulations. In order to deal with the time restrictions of the project, we used a high resistivity (HR) Si wafer and altered the process flow (see section 5.1). Indeed, CMi's SPIDER 600 was not available for the SiO2 deposition. Thus, we decided to only use the ebeam resist in step 14.[3] Moreover, the dicing of the chips take a few days that we did not have. Subsequently, the process flow of this test devices is similar as the one presented in section 5.1 with the omission of steps 8, 9, 11 and 13.

The manufactured devices were measured in ANEMS laboratory. Unfortunately, any acoustic response has been recorded. We attribute this disfunctionment to the bad lift-off conditions during step 03. Because CMi's charts were outdated, extreme doses (80 $[J \cdot cm^{-2}]$ instead of 46 $[J \cdot cm^{-2}]$) were used during the exposition of the photoresist (step 01). Subsequently, the profile of the bottom electrode after lift-off (see fig. 5.4) presents 200nm-high peaks on its sides. We think that this irregularity may lead to a higher resistance than expected. Another hypothesis is the high resistivity of thin (< 50 $[nm]$) Ti layers. Indeed, a similar observation has been done by ANEMS with Mo thin films.

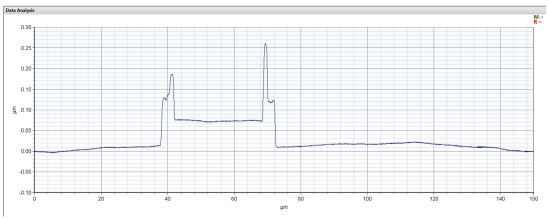

Figure 5.4: Profile of the bottom electrode after the lift-off of HR01. Measured by Damien Maillard (ANEMS) in CMi with the mechanical surface profiler: Bruker Dektak XT. Wafer: HR01, device unknown.

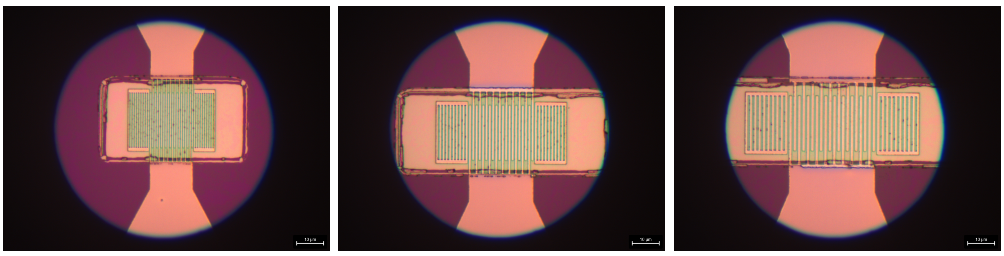

(a)

(b) (c)

Figure 5.5: Optical observation of the manufactured test devices. The observation has de done in CMi's cleanroom with an optical microscope. (a) $pitch = 0.8$ $[um]$; (b) $pitch = 1.2$ $[um]$; (c) $pitch = 1.6$ $[um]$. As presented in figure 5.4, we notice the irregularity of the edge of the bottom electrode.

[3] The only limitation of not using the oxide layer is the maximum etching depth in step 14.

Chapter 6

Conclusion

AlN and AlScN are described in the literature as the best piezoelectric materials for harsh environment sensing.
In this study, d_{33} has been identified as the main exited mode during the generation of SAW in AlScN thin films. Subsequently, an increase of the electromechanical coupling factor has been predicted in the presence of a bottom electrode.
To increase further the FoM, traditional SAW resonators has been ruled out in profit of a SAW/BAW hybrid design. A parametric study has shown the potential of such hybrids and build a data base allowing a future modelization of their underlying mechanisms. With unprecedented records in the literature, we also noticed that the optimal thickness-over-pitch ratio shifts within the etching of the piezoelectric layer.
The four best designs have been studied further with a FD simulation. Through this study, we have shown the ability of 2λ-periodic reflectors to confine the acoustic waves within the IDT and confirmed the performances of these designs.

With a higher electromechanical coupling factor than SAW resonators and a quality factor comparable to BAW and Lamb resonators, SAW/BAW hybrid resonators display the highest FoM ever recorded : $FoM_{AlN} = 48$ [−], $FoM_{AlSc(0.17)N} = 105$ [−], $FoM_{AlSc(0.40)N} = 494$ [−].

Thanks to its incredible performances and high frequency capabilities, hybrid designs are not limited to harsh environment sensing but may became, in a near future, a high-potential candidate for a wide range of applications such as high frequency filters for telecommunication.

Objective	Status	Remarks
A01	Achieved	Through its literature review, UC and FD simulations, this thesis demonstrates the potential of AlN/AlScN based resonators for harsh environment sensing.
A02	Achieved	Our parametric study has highlighted few devices with high FoM. The FD simulation has confirmed the performance of these designs.
A03	Achieved	A process flow has been accepted by CMi and a first chip has been manufactured.
B01	Achieved	We demonstrate that AlSc(0.40)N hybrid resonators with high FoM operates at 2.4 $[GHz]$. Moreover, the parametric study shows our capability to fine tune this frequency if needed.
B02	On going	A chip of HR-Si-01 has been manufactured but it was not functional. Two wafers (HR-Si-02 and SiC-01) are currently in process.
B03	Mixed Progress	The temperature behavior of AlN/AlScN has been demonstrated in the literature but any simulation has been ran yet.
C01	Not Achieved	No theoretical model has been developed for hybrid SAW/BAW resonators.
C02	Mixed Progress	We optimized the standing wave configuration. But any of the studied designs has shown a high propagation of SAW.
C03	Not Achieved	No functional device has been manufactured yet.

Table 6.1: Status of the Objectives on mid-January 2021

Bibliography

[1] Z. Hao, M. Park, D. G. Kim, A. Clark, R. Dargis, H. Zhu, and A. Ansari. Single crystalline scaln surface acoustic wave resonators with large figure of merit $(q \cdot k_t^2)$. In *2019 IEEE MTT-S International Microwave Symposium (IMS)*, pages 786–789, 2019.

[2] Jiuping Xu and Lei Xu. *Integrated System Health Management, Perspectives on Systems Engineering Techniques.* 2017.

[3] H. Campanella. *Acoustic Wave and Electromechanical Resonators: Concept to Key Applications.* 2010.

[4] Shujun Zhang, Ru Xia, Laurent Lebrun, Dean Anderson, and Thomas R. Shrout. Piezoelectric materials for high power, high temperature applications. *Materials Letters*, 59(27):3471 – 3475, 2005.

[5] A. Teshigahara, K. Hashimoto, and M. Akiyama. Scandium aluminum nitride: Highly piezoelectric thin film for rf saw devices in multi ghz range. In *2012 IEEE International Ultrasonics Symposium*, pages 1–5, 2012.

[6] Andrea Lozzi, Marco Liffredo, Ernest Ting-Ta Yen, Jeronimo Segovia-Fernandez, and Luis Guillermo Villanueva. Evidence of smaller 1/f noise in alscn-based oscillators compared to aln-based oscillators. *Journal Of Microelectromechanical Systems*, 29(3):306–312, 2020.

[7] Hong hoang si and Gwiy-Sang Chung. Eect of thermal annealing on the saw properties of aln films deposited on si substrate. *Journal- Korean Physical Society*, 54:1519–1525, 04 2009.

[8] Thierry Aubert, Omar Elmazria, Badreddine Assouar, Laurent Bouvot, and Mourad Oudich. Surface acoustic wave devices based on aln/sapphire structure for high temperature applications. *Applied Physics Letters*, 96(20):203503, 2010.

[9] Thierry Aubert, Jochen Bardong, Ouarda Legrani, Omar Elmazria, M. Badreddine Assouar, Gudrun Bruckner, and Abdelkrim Talbi. In situ high-temperature characterization of aln-based surface acoustic wave devices. *Journal of Applied Physics*, 114(1):014505, 2013.

[10] F. Bartoli, M. Moutaouekkil, J. Streque, P. Pigeat, S. Hage-Ali, P. Boulet, H. M'Jahed, O. Elmazria, S. Zhgoon, F. Bartoli, T. Aubert, O. B. Matar, and A. Talbi. Theoretical and experimental study of scaln/sapphire structure based saw sensor. In *2017 IEEE SENSORS*, pages 1–3, 2017.

[11] Chih-Ming Lin, Ting-Ta Yen, Valery V. Felmetsger, Matthew A. Hopcroft, Jan H. Kuypers, and Albert P. Pisano. Thermally compensated aluminum nitride lamb wave resonators for high temperature applications. *Applied Physics Letters*, 97(8):083501, 2010.

[12] Ieee standard on piezoelectricity. *ANSI/IEEE Std 176-1987*, pages 0_1–, 1988.

[13] Shang Gao, Xuewu Dai, Yu Hang, Yuyan Guo, and Qian Ji. Airborne wireless sensor networks for airplane monitoring system. *Wireless Communications and Mobile Computing*, 2018, 05 2018.

[14] K. Uchino. *Advanced Piezoelectric Materials (Second Edition)*. Woodhead Publishing in Materials. Woodhead Publishing, second edition edition, 2017.

[15] Qingming Chen and Qing-Ming Wang. The effective electromechanical coupling coefficient of piezoelectric thin-film resonators. *Applied Physics Letters*, 86(2):022904, 2005.

[16] James M. Lehto Miller, Azadeh Ansari, David B. Heinz, Yunhan Chen, Ian B. Flader, Dongsuk D. Shin, L. Guillermo Villanueva, and Thomas W. Kenny. Effective quality factor tuning mechanisms in micromechanical resonators. *Applied Physics Reviews*, 5(4):041307, 2018.

[17] R. Priya, Venkatesan Thirumal, G Pandiyarajan, and Haresh Pandya. A short review of saw sensors. *Journal of Environmental Nanotechnology*, 4, 12 2015.

[18] R. M. White and F. W. Voltmer. Direct piezoelectric coupling to surface elastic waves. *Applied Physics Letters*, 7(12):314–316, 1965.

[19] F. Schmidt, O. Sczesny, L. Reindl, and V. Magori. Remote sensing of physical parameters by means of passive surface acoustic wave devices ("id-tag"). In *1994 Proceedings of IEEE Ultrasonics Symposium*, volume 1, pages 589–592 vol.1, 1994.

[20] L. Reindl, G. Scholl, T. Ostertag, C. C. W. Ruppel, W. . Bulst, and F. Seifert. Saw devices as wireless passive sensors. In *1996 IEEE Ultrasonics Symposium. Proceedings*, volume 1, pages 363–367 vol.1, 1996.

[21] Lin Shu, Bin Peng, Chuan Li, Dongdong Gong, Zhengbing Yang, Xingzhao Liu, and Wanli Zhang. The characterization of surface acoustic wave devices based on aln-metal structures. *Sensors*, 16:526, 04 2016.

[22] Chen Fu, Yabing ke, Min Li, Jim(Jingting) Luo, Honglang Li, Guangxing Liang, and Fan Ping. Design and implementation of 2.45 ghz passive saw temperature sensors with bpsk coded rfid configuration. *Sensors*, 17:1849, 08 2017.

[23] O. Tigli and M. E. Zaghloul. Design, modeling, and characterization of a novel circular surface acoustic wave device. *IEEE Sensors Journal*, 8(11):1807–1815, 2008.

[24] A. Ansari. Single crystalline scandium aluminum nitride: An emerging material for 5g acoustic filters. In *2019 IEEE MTT-S International Wireless Symposium (IWS)*, pages 1–3, 2019.

[25] Wenbo Wang, Patrick M. Mayrhofer, Xingli He, Manuel Gillinger, Zhi Ye, Xiaozhi Wang, Achim Bittner, Ulrich Schmid, and J. K. Luo. High performance alscn thin film based surface acoustic wave devices with large electromechanical coupling coefficient. *Applied Physics Letters*, 105(13):133502, 2014.

[26] Cristian Cassella, Yu Hui, Zhenyun Qian, Gwendolyn Hummel, and Matteo Rinaldi. Aluminum nitride cross-sectional lamé mode resonators. *Journal of Microelectromechanical Systems*, 25:1–11, 01 2016.

[27] Soumya Yandrapalli, David Ruffieux, and Luis G. Villanueva. Three-dimensional nano-acoustic bragg reflectors for cmos embedded nems. *IEEE Transactions On Nanotechnology*, 16(4):6. 653–658, 2017.

[28] J. B. Shealy, R. Vetury, S. R. Gibb, M. D. Hodge, P. Patel, M. A. McLain, A. Y. Feldman, M. D. Boomgarden, M. P. Lewis, B. Hosse, and R. Holden. Low loss, 3.7ghz wideband baw filters, using high power single crystal aln-on-sic resonators. In *2017 IEEE MTT-S International Microwave Symposium (IMS)*, pages 1476–1479, 2017.

[29] V. Pashchenko, R. Matloub, F. Parsapourkolour, P. Muralt, S. Ballandras, and K. Haffner. Hybrid baw/saw aln and alscn thin film resonator. In *2016 IEEE International Ultrasonics Symposium (IUS)*, pages 1–4, 2016.

[30] V. Pashchenko, M. F. P. Kolour, S. Ballandras, and P. Muralt. Effective saw excitation on the non-piezoelectric substrate using the alscn piezoelectric film baw/saw hybrid transducer. In *2017 IEEE International Ultrasonics Symposium (IUS)*, pages 1–1, 2017.

[31] K. Hashimoto, S. Sato, A. Teshigahara, T. Nakamura, and K. Kano. High performance surface acoustic resonators in 1–3 ghz range using scaln/6h-sic structure. In *2012 IEEE/MTT-S International Microwave Symposium Digest*, pages 1–3, 2012.

[32] K. Hashimoto, T. Fujii, S. Sato, T. Omori, Changjun Ahn, A. Teshigahara, K. Kano, H. Umezawa, and S. Shikata. High q surface acoustic wave resonators in 2–3 ghz range using scaln/single crystalline diamond structure. In *2012 IEEE International Ultrasonics Symposium*, pages 1–4, 2012.

[33] Andrea Lozzi, Ernest Ting-Ta Yen, Paul Muralt, and Luis Guillermo Villanueva. Al0.83sc0.17n contour-mode resonators with electromechanical coupling in excess of 4.5 *IEEE Transactions On Ultrasonics Ferroelectrics And Frequency Control*, 66(1):146–153, 2019.

[34] A. Ballato and J. G. Gualtieri. Advances in high-q piezoelectric resonator materials and devices. *IEEE Transactions on Ultrasonics, Ferroelectrics, and Frequency Control*, 41(6):834–844, 1994.

[35] Marc-Alexandre Dubois and Paul Muralt. Stress and piezoelectric properties of aluminum nitride thin films deposited onto metal electrodes by pulsed direct current reactive sputtering. *Journal of Applied Physics*, 89(11):6389–6395, 2001.

Appendices

Appendix A

Material Properties of AlScN used in the simulations

A.1 Material data of AlSc(0.4)N

Property	Unit	Value
Density	$kg \cdot m^3$	3680
Relative permittivity	$-$	15

Table A.1: Relevant properties of AlSc(0.40)N for the simulation setup.

0	0	0	0	-0.24942[C/m^2]	0
0	0	0	0	0	0
-0.73198[C/m^2]	-0.73198[C/m^2]	2.72882[C/m^2]	0	0	0

Figure A.1: Coupling Matrix of AlSc(0.40)N. Screenshot of COMSOL's GUI.

298.068e9	143.274e9	132.196e9	0	0	0
143.274e9	298.068e9	132.196e9	0	0	0
132.196e9	132.196e9	183.394e9	0	0	0
0	0	0	103.338e9	0	0
0	0	0	0	103.338e9	0
0	0	0	0	0	76e9

Figure A.2: Elasticity Matrix of AlSc(0.40)N. Screenshot of COMSOL's GUI.

A.2 Material data of AlSc(0.17)N

Property	Unit	Value
Density	$kg \cdot m^3$	3453.8
Relative permittivity	–	13

Table A.2: Relevant properties of AlSc(0.17)N for the simulation setup.

0	0	0	0	-0.3019198[C/m...	0
0	0	0	-0.48[C/m^2]	0	0
-0.64926395[C/...	-0.64926395[C/...	1.7649268[C/m...	0	0	0

Figure A.3: Coupling Matrix of AlSc(0.17)N. Screenshot of COMSOL's GUI.

345.29367e9[Pa]	136.46991e9[Pa]	118.55079e+9[Pa]	0	0	0
136.46991e9[Pa]	345.29367e9[Pa]	118.55079e+9[Pa]	0	0	0
118.55079e+9[Pa]	118.55079e+9[Pa]	287.44646e+9[Pa]	0	0	0
0	0	0	106.19897e+9[Pa]	0	0
0	0	0	0	106.19897e+9[Pa]	0
0	0	0	0	0	76e9[Pa]

Figure A.4: Elasticity Matrix of AlSc(0.17)N. Screenshot of COMSOL's GUI.

Appendix B

Complete Simulation Setup Description

B.1 Mechanical Environment

Condition	Parameters	
Linear Elastic Material 1	Solid Model : isotropic ; Material damping : isotropic loss factor ($\eta_s = 0.002$)	Domain : Electrodes
Linear Elastic Material 2	Solid Model : isotropic ; Material damping : isotropic loss factor (Si:η_s = 0.0005 - SiC/SCD :$\eta_s = 0.0002$)	Domain : Substrate
Piezoelectric Material 1	Coordinate System : Material XZ-Plane System ; Piezoelectric Constitutive relation : Stress-Charge form ; Remanent electric displacement : $D_r = [0; 0; 0]$; Material damping : isotropic loss factor ($\eta_s = 0.00035$)	Domain : Piezoelectric layer
Periodic Condition	Type of periodicity: Continuity	Edges: Left and right vertical edges
Free	-	Edge : Air/Solid Interface
Fixed constraint	-	Edge: Bottom edge of the PML.
Initial Value	$\mathbf{u} = [0, 0]^T$ $[m]$; $\frac{\partial \mathbf{u}}{\partial t} = [0, 0]^T$ $[m \cdot s^{-1}]$	Domain : All

Table B.1: Description of mechanical conditions for the UC simulation

B.2 Electrostatics Environment

Condition	Parameters	
Charge Conservation 1	Material type: Nonsolid ; Constitutive relation: relative permittivity	Domain: All air domains
Charge Conservation 2	Material type: Solid ; Constitutive relation: relative permittivity	Domain: Substrate & bottom electrode
Charge Conservation, Piezoelectric 1	-	Domain: Piezoelectric layer
Periodic Condition	Type of periodicity: Continuity	Edges: Left and right vertical edges
Zero Charge	-	Edge: Top edge of Air
Ground 1	-	Edge: Bottom edge of Substrate (interface with PML)
Floating Potential 1	Charge : $Q_0 = 0$ $[C]$; Initial value for voltage : $V_{init} = 0$ $[V]$	Edge: All edges of the bottom electrode
Terminal 1	Voltage: $V_0 = -1$ $[V]$	Domain: Left electrode (IDT)
Terminal 2	Voltage: $V_0 = +1$ $[V]$	Domain: Right electrode (IDT)
Initial Values1	Electric potential: $V = 0$ $[V]$	Domain: All

Table B.2: Description of electrostatic conditions for the UC simulation

Appendix C

Relation between frequency, substrate and bottom electrode

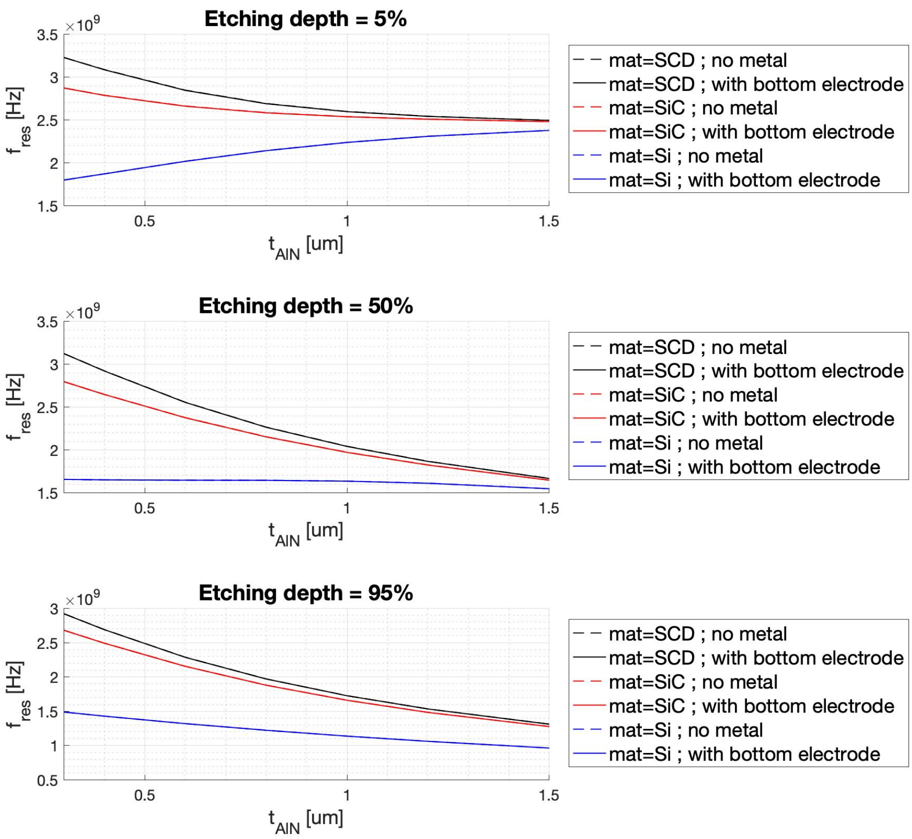

Figure C.1: Impact of the substrate and bottom electrode onto first mode's resonance frequency (f_{res}) in function of AlN thickness

Simulation parameters : pitch $= 1.0$ $[\mu m]$*;* $t_{Pt} = 50$ $[nm]$*; coverage* $= 50$ $[\%]$*; Substrate=SiC*

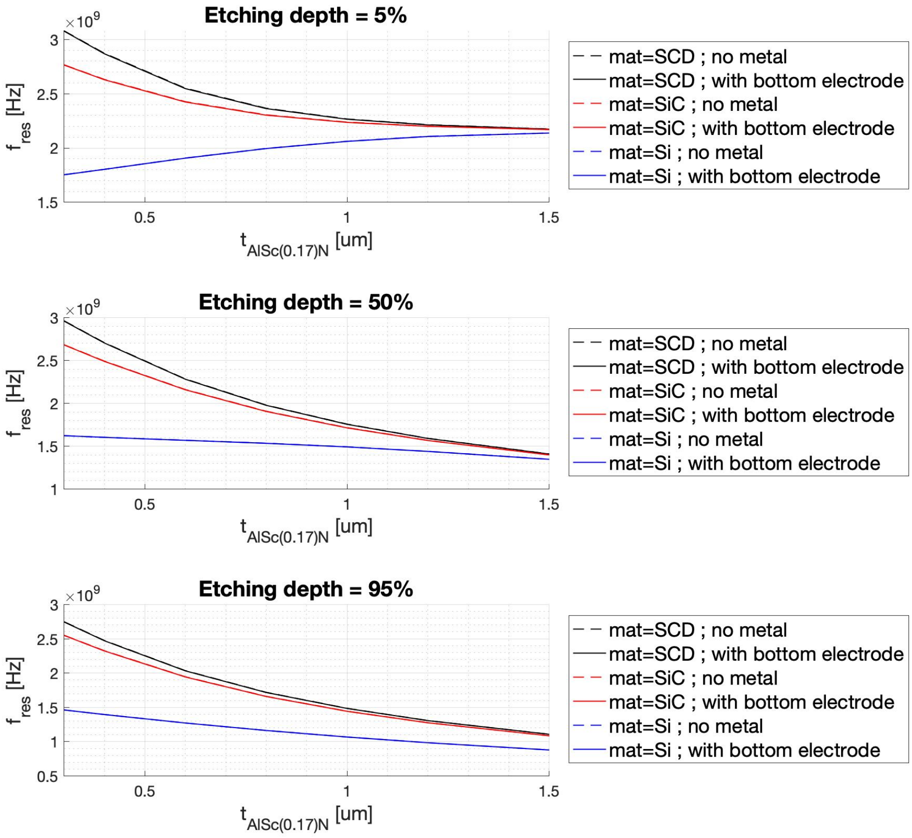

Figure C.2: Impact of the substrate and bottom electrode onto first mode's resonance frequency (f_{res}) in function of AlSc(0.17)N thickness

Simulation parameters : pitch $= 1.0$ $[\mu m]$; $t_{Pt} = 50$ $[nm]$; *coverage* $= 50$ $[\%]$; *Substrate=SiC*

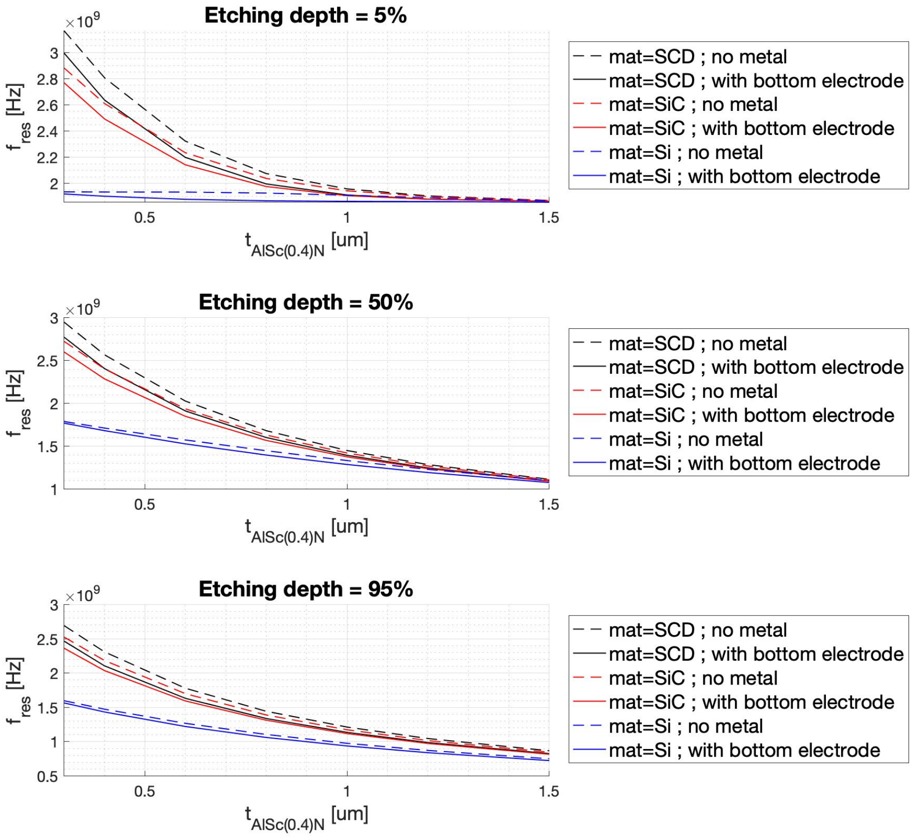

Figure C.3: Impact of the substrate and bottom electrode onto first mode's resonance frequency (f_{res}) in function of AlSc(0.4)N thickness

Simulation parameters : pitch $= 1.0$ $[\mu m]$*;* $t_{Pt} = 50$ $[nm]$*; coverage* $= 50$ $[\%]$*; Substrate=SiC*